The Evolution of Mesoscale Vortex Impinging on Symmetric Topography

CHING-YUANG HUANG* AND YUH-LANG LIN**

*Department of Atmospheric Sciences
National Central University
Chung-Li, Taiwan, R.O.C.
**Department of Marine, Earth, and Atmospheric Sciences
North Carolina State University
Raleigh, NC, U.S.A.

ABSTRACT

This study employed a mesoscale numerical model to investigate the evolution of a mesoscale vortex impinging on symmetric topography. The numerical model consists of higher-order planetary boundary layer parameterization, cloud microphysics and an initialization method for typhoon simulations. For long typhoon simulation time, the numerical model employs highly accurate high-order semi-Lagrangian schemes to reduce the numerical damping. Numerical results from idealized case simulations tend to show that a westbound vortex as in a smaller typhoon, slow or fast and weak or intense, will be deflected southward rather than northward as it approaches the center of a symmetric topography and will then rebound slightly northward to its original latitude after passing the mountain.

Momentum budget analyses indicate that the mechanism most probably responsible for the southward deflection is the southward component of the ageostrophic pressure gradient. As the vortex center approaches the island, it is also retarded by the eastward component of the ageostrophic pressure gradient. In the mean time, a secondary low is induced at the lee side of the mountain associated with a strong downslope wind favorable for vorticity generation. The lee secondary low is replaced by the original vortex center which considerably accelerates after turning around the mountain peak. The reformed low center then moves straight westward at later times.

Key Words: typhoon, deflection, westbound vortex, secondary low, downslope wind

I. Introduction

Typhoons and Mei-Yu fronts are two of the major severe types of weather associated with heavy rainfall in Taiwan. Moreover, floods caused by intense impinging typhoons have the greatest impact on the island. Typhoon Herb in July, 1996, the most impressive recent event, caused agricultural and economic loses of more than 50 billion NT dollars (~ 2 billion US dollars) as estimated by the government. Statistically, the yearly average precipitation is about 2500 mm, almost half of which is brought by typhoon circulation systems. This observational data may explain some draught years in which typhoons do not shoot around the island. On the other hand, the landfall position of a typhoon center is closely indicative of the locations associated with heavy rainfall. Typhoon track forecasting has been a central issue for the typhoon research group of the Central Weather Bureau (CWB) (Peng, 1992).

Observations on upstream maritime typhoons before they impinge on Taiwan have usually been very insufficient for confident analyses. Despite this observational drawback, Brand and Blelloch (1974) conducted statistical analyses of westbound typhoons impinging on Taiwan that exhibited a northward deflection and reduced intensity as they approached the island while the center appeared to accelerate after landing. An extensive observational study of 120 typhoons by Wang (1980) suggested that the typhoon track may be continuous or discontinuous (Fig. 1) when a westward typhoon impinges on the island at a certain angle. A detailed analysis of track deflection and translational speed for westward typhoons was given by Yeh and Elsberry (1993a). They found that the increase in the along-track translational speed prior to landfall for stronger and faster typhoons was more evident than that for weaker and slower typhoons. The effects of Taiwan's topography on the evolution of typhoon circulations were also analyzed by Lee (1991) and Tsay (1993), both of whom suggested an important role for the topography.

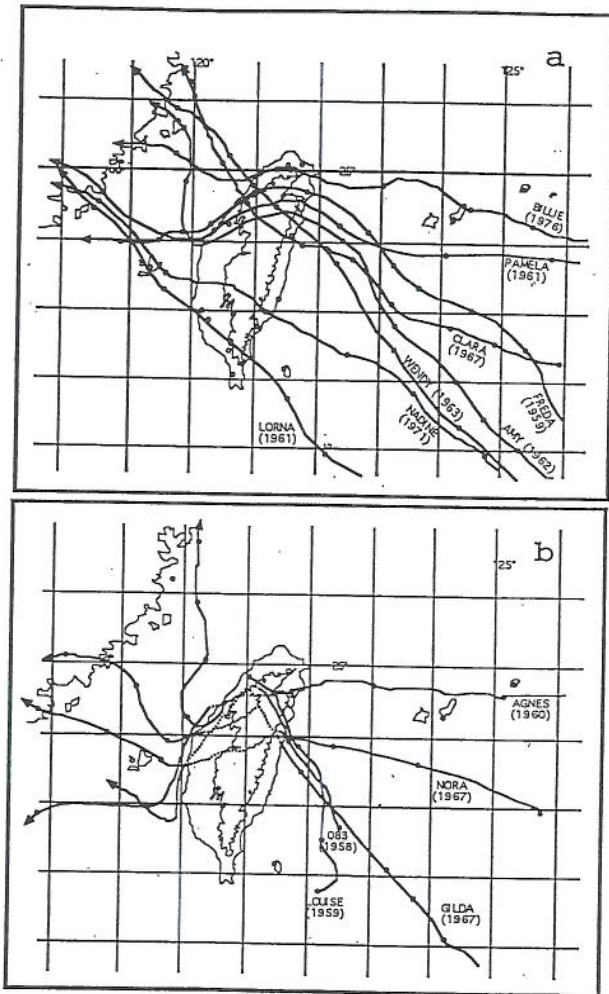Several numerical studies have also shown track

Fig. 1. Two types of typhoon tracks: (a) Continuous and (b) discontinuous (after Wang, 1980).

deflection of a westward typhoon toward the Taiwan island. Chang (1982) found that a typhoon somewhat larger than the size of the island tended to be deflected northward and to accelerate prior to landfall; thus, its track exhibited a cyclonic curvature. It was speculated that the northward deflection was related to more latent heat release to the right of the center as the northern cyclonic flow was lifted by the terrain. Bender *et al.* (1987) also found that westward typhoons appeared to turn rightward in the presence of β-effects, which are known to drive the vortex poleward and westward (e.g., Fiorino and Elsberry, 1989). The northward deflection was also exhibited in the modeling study of Yeh and Elsberry (1993a, 1993b) and was explained by the asymmetric southerly flow crossing the island. They also investigated the generation mechanisms of observed secondary-low centers using a primitive-equation numerical model. For weaker typhoons, a secondary low was induced on the lee side of the mountain while the upstream low center was blocked. The

secondary circulation center on the lee side of the island was also very evident in the real case simulations of Typhoon Dot [1990] carried out using the NCAR MM5 model (Cho *et al.*, 1996) and of Typhoon Gladys [1989] using the GFDL hurricane model (Wu and Chuo, 1996).

Both modeling results (e.g., Yeh and Elsberry, 1993a) and observations (e.g., Wang, 1980) indicated northward (southward) track deflection for westbound typhoons impinging on the northern (southern) part of the island. Some modeling and more observational evidence indicated northward deflection for typical tracks moving toward the central point of the topography, but there was also a possibility of southward deflection in this case, e.g., Typhoon Nora [1967] and Nadine [1971], as shown in Fig. 1. No attempt was made to dynamically or observationally identify the possibility of southward or northward deflection for real cases.

While considerable observational and modeling efforts have been made in the study of typhoon track evolution in the vicinity of Taiwan, a comprehensive typhoon numerical model still needs to be developed in Taiwan for scientific investigation. Using a native typhoon model, this study will show that a southward deflection prior to landfall can be associated with smaller typhoons, whether strong or weak, slow or fast. Although we will not frequently expect a westbound impinging typhoon to move toward the central point of the CMR despite its asymmetric topography, an understanding of the basic behavior of track deflection with comprehensive interpretation is needed. Since many physical parameters are involved in numerical experiments, we will concentrate on cases with idealized topography and simple initial conditions. Also, there are many issues that can be examined in numerical simulations; however, we will limit our focus to vortex evolution and track deflection. Cloud and rain development processes will not be discussed for this reason; a detailed presentation can be found in Huang (1993). In Section II, the mesoscale numerical model is introduced together with the typhoon initialization scheme. The modeling results are presented in Section III, followed by our discussion in Section IV. Brief conclusions are given in the last section.

II. The Numerical Model

1. The Governing Equations

The mesoscale model used in this study was described by Huang (1993). The model is anelastic and hydrostatic or nonhydrostatic in a terrain-following coordinate system with Boussinesq's approximation. Since the vortex circulations studied herein are not too

tiny in size to invalidate the hydrostatic approximation, all the simulations in this study have used the hydrostatic version for computational efficiency.

The model momentum equations in the z-coordinate are given by

$$u_t=-uu_x-vu_y-wu_z+fv-\theta_v\pi_x+(K_Hu_x)_x+(K_Hu_y)_y$$

$$+(K_Mu_z)_z, \tag{1}$$

$$v_t=-uv_x-vv_y-wv_z-fu-\theta_v\pi_y+(K_Hv_x)_x+(K_Hv_y)_y$$

$$+(K_Mv_z)_z, \tag{2}$$

$$w_t=-uw_x-vw_y-ww_z-\theta_v\pi_z-g+(K_Hw_x)_x+(K_Hw_y)_y$$

$$+(K_Mw_z)_z, \tag{3}$$

where K_H and K_M are the horizontal and vertical eddy diffusivities, respectively. The deep continuity equation used in the model can be written as

$$(\rho_0u)_x+(\rho_0v)_y+(\rho_0w)_z=0, \tag{4}$$

where $\rho_0=\rho_0(z)$ is the layer-average density, which only depends on height.

The scaled pressure π (Exner function) is derived from

$$\pi=C_p\left(\frac{P}{P_{00}}\right)^\kappa,$$

where $\kappa=R/C_p$, R is the gas constant and C_p is the specific heat capacity at constant pressure. The virtual potential temperature θ_v is defined as

$$\theta_v=\theta(1+0.61q-q_c-q_r),$$

where q is the water vapor, q_c the cloud water and q_r the rain water. In Eqs. (1) and (2), the pressure terms can be further linearized by replacing θ_v with θ_{v0} (the ambient geostrophic value). The pressure can also be partitioned into two parts, the hydrostatic and geostrophic pressure π_0, and the non-geostrophic pressure perturbation π' (hydrostatic or non-hydrostatic):

$$\pi=\pi_0+\pi', \quad \pi_{0z}=-\frac{g}{\theta_{v0}}. \tag{5}$$

Hence, the momentum equations can be given by

$$u_t=-uu_x-vu_y-wu_z+(fv-fv_g)-\theta_{v0}\pi'_x+(K_Hu_x)_x$$

$$+(K_Hu_y)_y+(K_Mu_z)_z, \tag{6}$$

$$v_t=-uv_x-vv_y-wv_z-(fu-fu_g)-\theta_{v0}\pi'_y+(K_Hv_x)_x$$

$$+(K_Hv_y)_y+(K_Mv_z)_z, \tag{7}$$

$$w_t=-uw_x-vw_y-ww_z-\theta_{v0}\pi'_z+g\frac{\theta'}{\theta_{v0}}+(K_Hw_x)_x+(K_Hw_y)_y$$

$$+(K_Mw_z)_z. \tag{8}$$

The vertical coordinate in the terrain-following coordinate system is defined as

$$\sigma=\frac{z-E(x,y)}{H-E(x,y)}, \tag{9}$$

where $E(x,y)$ is the terrain height above sea level, and H is the fixed height of the model domain top. The transformed governing equations, including thermodynamic and mass-conservative equations, are given by

$$u_t=-uu_x-vu_y-\tilde{w}u_\sigma+(fv-fv_g)-\theta_{v0}(\pi'_x+\pi'_\sigma\sigma_x)+H_u+D_u, \tag{10}$$

$$v_t=-uv_x-vv_y-\tilde{w}v_\sigma-(fu-fu_g)-\theta_{v0}(\pi'_y+\pi'_\sigma\sigma_y)+H_v+D_v, \tag{11}$$

$$w_t=-uw_x-vw_y-\tilde{w}w_\sigma-\theta_{v0}\pi'_\sigma\sigma_z+g\frac{\theta'}{\theta_{v0}}+H_w+D_w, \tag{12}$$

$$[\rho_0u(H-E)]_x+[\rho_0v(H-E)]_y+[\rho_0\tilde{w}(H-E)]_\sigma=0, \tag{13}$$

$$\theta_t=-u\theta_x-v\theta_y-\tilde{w}\theta_\sigma-Q_{CN}+Q_{CL}-Q_{EV}+Q_{RAD}+H_\theta+D_\theta, \tag{14}$$

$$q_t=-uq_x-vq_y-\tilde{w}q_\sigma-M_{CN}+M_{CL}+M_{EV}+H_q+D_q, \tag{15}$$

$$q_{ct}=-uq_{cx}-vq_{cy}-\tilde{w}q_{c\sigma}+M_{CN}-M_{AC}-M_{RV}+H_{qc}+D_{qc}, \tag{16}$$

$$q_{rt}=-uq_{rx}-vq_{ry}-\tilde{w}q_{r\sigma}+M_{VT}+M_{AC}+M_{RV}-M_{EV}+H_{qr}$$

$$+D_{qr}, \tag{17}$$

where Eq. (14) is the thermodynamic equation for potential temperature; Eqs. (15), (16) and (17) the conservative equations for water vapor, cloud water and rain water, respectively. When the hydrostatic approximation is used, Eq. (12) retains only two terms, the vertical pressure perturbation gradient and the buoyancy force; otherwise, the anelastic continuity equation Eq. (13) is used to derive the pressure perturbation to eliminate the sound wave mode. The σ-coordinate vertical velocity $\tilde{w}(=d\sigma/dt)$ can be related to the vertical velocity $w(=dz/dt)$ as $w=\tilde{w}(H-E)-(\sigma-1)(uE_x+vE_y)$. In the above prognostic equations, the diffusion terms are

defined as

H_u: horizontal u-momentum flux divergences in the x- and y-directions,

D_u: vertical u-momentum flux divergence in the z-direction,

H_v: horizontal v-momentum flux divergences in the x- and y-directions,

D_v: vertical v-momentum flux divergence in the z-direction,

and so on. Since the mathematical expansions of the diffusion terms in the σ-coordinate are very lengthy, the detailed expressions are omitted herein. The spatial x-, y- and z-derivatives of the vertical coordinate are

$$\sigma_x = \frac{\sigma - 1}{(H - E)} E_x , \qquad (18a)$$

$$\sigma_y = \frac{\sigma - 1}{(H - E)} E_y , \qquad (18b)$$

$$\sigma_z = \frac{1}{(H - E)} , \qquad (18c)$$

respectively.

The Ertel's potential vorticity (PV) in the z-coordinate can be defined as $PV = (1/\rho)(f\mathbf{k} + \nabla \times \mathbf{V}) \cdot \nabla \theta$, which can be expanded after neglecting the density variation as

$$PV = \frac{\partial \theta}{\partial x}\left(\frac{\partial w}{\partial y} - \frac{\partial v}{\partial z}\right) + \frac{\partial \theta}{\partial y}\left(\frac{\partial u}{\partial z} - \frac{\partial w}{\partial x}\right) + \frac{\partial \theta}{\partial z}\left(\frac{\partial v}{\partial x} - \frac{\partial u}{\partial y} + f\right). \qquad (19)$$

With the σ-coordinate in this study, the vertical component of the relative vorticity ζ in the last parentheses of Eq. (19) can be expressed as $v_x + v_\sigma\sigma_x - u_y - u_\sigma\sigma_y$. In later analyses, the formulation of PV will also be transformed to the σ-coordinate.

The sink or source terms in Eqs. (14)-(17) are described below:

Q_{CN}: release rate of latent heat by condensation of water vapor at grid points,

Q_{CL}: release rate of latent heat by condensation of water vapor in subgrid scale clouds,

Q_{EV}: release rate of latent heat by evaporation of rain water,

Q_{RAD}: radiational cooling or heating,

M_{CN}: moisture contribution due to condensation of water vapor at grid points,

M_{CL}: moisture contribution due to condensation of water vapor in subgrid clouds,

M_{EV}: moisture contribution from evaporation of rain water,

M_{VT}: falling rate of raindrops by terminal velocity,

M_{AC}: accretion of cloud water to become rain drops,

M_{RV}: reverted rain water due to autoconversion of cloud water.

The above physical cloud processes are based on Kessler (1969) and can be found in Huang (1990).

The atmospheric PBL is treated separately as the surface layer and the transition layer. The similarity stability functions given by Businger *et al.* (1971) are used to account for the surface-layer turbulent transport. Above the surface layer, a turbulence closure scheme (K-theory) based on the prognostic equation of turbulent kinetic energy (e) and energy dissipation (ε) is incorporated with the level 2.5 scheme of Mellor and Yamada (1982) to determine eddy diffusivities, K_M and K_θ, in the transition layer. The prognostic equations for TKE and ε (see Duynkerke and Driedonks, 1987) are given by

$$\frac{\partial e}{\partial t} = -\overline{V} \cdot \overline{\nabla} e + \left[-\overline{u'w'}\frac{\partial u}{\partial z} - \overline{v'w'}\frac{\partial v}{\partial z} + \frac{g}{\theta_0}\overline{w'\theta_v'}\right]$$

$$- \frac{\partial \overline{w(e' + p'/\rho_0)}}{\partial z} - \varepsilon ,$$

and $\qquad\qquad\qquad\qquad\qquad\qquad (20)$

$$\frac{\partial \varepsilon}{\partial t} = -\overline{V} \cdot \overline{\nabla}\varepsilon + c_3\frac{\varepsilon}{E}\left[-\overline{u'w'}\frac{\partial u}{\partial z} - \overline{v'w'}\frac{\partial v}{\partial z} + \frac{g}{\theta_0}\overline{w'\theta_v'}\right]$$

$$- c_4\frac{\varepsilon^2}{E} + c_5\frac{\partial}{\partial z}\left(K_M\frac{\partial\varepsilon}{\partial z}\right), \qquad (21)$$

respectively, where C_3, C_4, and C_5 are constants (Duynkerke, 1988), K_θ is related to K_M as

$$K_\theta = P_r^{-1}K_M ,$$

and P_r is the turbulent Prandtl number determined in the level 2.5 closure. Using the predicted e and ε, K_M can be parameterized (see Huang, 1990).

The semi-Lagrangian advection scheme using seventh-order interpolation is adopted in the horizontal while cubic interpolation is employed in the vertical (for more details, see Huang, 1994). The Ekman-gradient wind is solved for the initial conditions used in the model (for more information, see Huang and Raman, 1989). Zero-gradient boundary conditions or radiation boundary conditions (Miller and Thorpe, 1981) of Orlanski's type (Orlanski, 1976) are used for all the prognostic variables at the lateral boundaries. A sponge layer is employed in the upper domain to absorb wave reflection. At the lower boundary, a no-slip condition is imposed for the wind.

2. Typhoon Initialization

A three-dimensional (3-D) wind field $\mathbf{V}$ can be

theoretically decomposed into two components, a non-divergent part, $\mathbf{V}_\psi$, and a irrotational part, $\mathbf{V}_e$, where

$$\nabla\cdot\mathbf{V}_\psi=0, \text{ and } \nabla\times\mathbf{V}_e=0. \qquad (22)$$

Observed typhoon circulations are essentially dominated by a rotational wind, which can be obtained from the gradient-wind balance equation. A 2-D wind field can be described by a streamfunction ψ such that

$$\mathbf{V}_\psi=\mathbf{k}\times\nabla\psi, \qquad (23)$$

and, thus,

$$u_\psi=-\frac{\partial\psi}{\partial y}, \quad v_\psi=\frac{\partial\psi}{\partial x}, \qquad (24)$$

which gives the vertical component of the relative vorticity vector:

$$\zeta=\mathbf{k}\cdot(\nabla\times\mathbf{V}_\psi)=\nabla^2\psi, \qquad (25)$$

which is the vorticity, which will be discussed later. Replacing the wind with the non-divergent wind, the horizontal momentum equation can be expressed as

$$\frac{\partial\mathbf{V}_\psi}{\partial t}+(\mathbf{V}_\psi\cdot\nabla)\mathbf{V}_\psi+f\mathbf{k}\times\mathbf{V}_\psi=-\theta_{v0}\nabla\pi', \qquad (26)$$

which is equivalent to

$$\frac{\partial\mathbf{V}_\psi}{\partial t}=-\nabla(\frac{\mathbf{V}_\psi\cdot\mathbf{V}_\psi}{2})-\theta_{v0}\nabla\pi'-\mathbf{k}\times\mathbf{V}_\psi(\zeta+f). \qquad (27)$$

Taking the divergence operation of Eq. (27), i.e., $\nabla\cdot(27)$, one obtains

$$\theta_{v0}\nabla^2[\pi']+\frac{1}{2}(\nabla\psi)^2_{,i}=\nabla\cdot[(f+\nabla^2\psi)\nabla\psi], \qquad (28)$$

which is the nonlinear balance equation dictating the relationship between the pressure and the wind. Once the streamfunction is known, Eq. (28) as a Poisson equation can be solved for the perturbation pressure, π'. However, the relationship between the horizontal pressure and the wind lacks a vertical link between each layer. In this study, the potential temperature perturbation is related to the pressure perturbation by the hydrostatic approximation as

$$\frac{\partial\pi'}{\partial z}=\frac{g\theta'}{\theta^2_{v0}}, \qquad (29)$$

where θ' is the potential temperature perturbation.

The steps of the typhoon initialization can be described in detail:

(1) Assume the 2-D tangential wind and then obtain the vorticity field;
(2) Use Eq. (25) to solve for the streamfunction with presumed zero circulation on the boundary;
(3) Use Eq. (24) to obtain the non-divergent wind field;
(4) Employ the alternating-direction-implicit (A.D.I.) method to solve Eq. (28) for the pressure perturbation on each vertical level;
(5) Use Eq. (29) to obtain the potential temperature perturbation;
(6) Set the environmental flow in thermal wind balance and obtain the steady-state Ekman-gradient wind using an 1-D PBL closure model (Huang and Raman, 1989);
(7) Superimpose the typhoon circulation on the environmental flow.

The initialization procedures first require a prescribed tangential wind field. In this study, the tangential wind following Chang (1982) is assumed to be

$$V_\theta=V_{max}(r/r_{max})\exp\{0.5[1-(r/r_{max})^2]\}, \qquad (30)$$

where V_{max} is the maximum tangential wind speed, and r_{max} is the radius to the vortex center. With Eq. (30), the vorticity is given by

$$\zeta=[2-(r/r_{max})^2](V_{max}/r_{max})\exp\{0.5[1-(r/r_{max})^2]\}, \qquad (31)$$

which determines the vortex to have negative vorticity at the radial larger than $\sqrt{2}\,r_{max}$ despite the fact that the tangential wind remains positive (i.e., counter-clockwise). The radial gradient of the tangential wind reflects the horizontal variation of the pressure perturbation while its vertical shear indicates the vertical pressure gradient and thus vertical potential temperature gradient. Usually, this simplification will result in a dynamically unbalanced 3-D vortex implanted into the full-primitive equation model since there is no inward or outward divergent (radial) component. The vortex is, however, quickly adjusted by producing flow divergence and vertical motions to redistribute the thermodynamic fields.

The typhoon vortex initialized by the above nonlinear balance equation used in most hurricane numerical models serves only as a first approximation of a real typhoon in the full-physics model, and the balanced typhoon should be obtained by model integration. Indeed, hurricane numerical models usually pre-run a set of cases for initial balanced flow that would take another equal computation time as for the model integration. The GFDL hurricane model uses

the simplified axis-symmetric version of the 3-D model to save computer time spent on initialization. A more feasible large-scale typhoon circulation (without the topography) could be obtained using the recently developed *PV* inversion technique for a balanced flow that exhibits reasonable 3-D hurricane structures (see Davis, 1992). However, this type of initialization scheme relies on specific model equations and cannot be immediately incorporated into the mesoscale model. It may be worthwhile to investigate the model performance using the new initialization scheme in the future, but at this time we will follow previous modeling studies (e.g., Yeh and Elsberry, 1993a, 1993b; Wu and Kurihara, 1996).

III. Results

In this study, the simulation domain is designed to include the entire typhoon circulation and the topography, both being put away to allow the vortex to have enough adjustment time prior to landfall. For all the cases presented in this paper, the grid numbers in the x, y and z directions $(NX, NY, NZ)=(120, 101, 30)$, respectively, with horizontal grid intervals of $\Delta x=20$ km and $\Delta y=20$ km. The time step of integration is chosen to be 60 s. Table 1 presents the vertical profiles of the vortex settings at each vertical level. Two vertical moisture profiles, the moist RH_1 and the dryer RH_1, are taken into account. We have found that the vortex development is sensitive to different ambient moisture conditions as should be expected, and that a dryer gradient-wind balanced vortex tends to decay gradually within one day. A stronger vortex requires more feasible ambient moisture profiles for justified development. This does not mean that the degree of moistening can be used to control the strength of the vortex, but instead that a stronger vortex will not allow an oversupply of moisture and, thus, latent heat if the dissipation is not increased in the model.

Five numerical experiments were conducted in this study and are briefly summarized in Table 2. A weaker typhoon was imposed in Case 1. Case 1F was the same as Case 1 except for a faster translational speed of the vortex. Case 1B was a sensitivity test on boundary conditions for Case 1 while Case 1G investigated the effects of non-separated pressure. All the cases of weaker typhoons employed the moisture profile of RH_1. Case 2 was for a stronger typhoon but with the moisture profile of RH_2 as described in Table 1. In all the above cases, an elliptical mountain was put on the grid (50, 51) with a peak height of 2.5 km. In addition, a land-sea contrast was included so that the topography represented an island geography. The coastline was defined at an elevation height of 10 cm.

Table 1. Vertical Profiles of the Implanted Vortex

Height (m)	V_{max}(m/s)	r_{max}(km)	$(I_c, J_c)^a$	θ (K)	RH_1^b(%)	RH_2^c(%)
0	20	120	(80, 51)	301.4	90	90
50	20	120	(80, 51)	300.4	90	90
100	20	120	(80, 51)	300.8	90	90
250	20	120	(80, 51)	301.4	90	90
500	20	120	(80, 51)	302.4	90	90
750	20	120	(80, 51)	303.4	90	90
1000	20	120	(80, 51)	304.4	90	90
1500	20	120	(80, 51)	306.4	90	50
2000	20	120	(80, 51)	308.4	90	50
2500	20	120	(80, 51)	310.4	90	50
3000	20	120	(80, 51)	312.4	90	50
3500	20	120	(80, 51)	314.4	90	50
4000	20	120	(80, 51)	316.4	90	50
4500	20	120	(80, 51)	318.4	90	50
5000	15	120	(80, 51)	320.4	90	50
6000	10	120	(80, 51)	324.4	90	50
7000	0	120	(80, 51)	328.4	90	50
8000	-5	120	(80, 51)	332.4	90	50
9000	-10	120	(80, 51)	336.4	70	50
10000	-5	120	(80, 51)	340.4	50	50
11000	0	120	(80, 51)	350.4	30	30
12000	0	120	(80, 51)	360.4	30	30
13000	0	120	(80, 51)	370.4	30	30
14000	0	120	(80, 51)	380.4	30	30
15000	0	120	(80, 51)	390.4	30	30
16000	0	120	(80, 51)	400.4	30	30
17000	0	120	(80, 51)	410.4	30	30
18000	0	120	(80, 51)	420.4	30	30
19000	0	120	(80, 51)	430.4	30	30
20000	0	120	(80, 51)	440.4	30	30

aThe horizontal location of the typhoon center.
b,cTwo vertical profiles of relative humidity.

Table 2. Descriptions of the Case Experiments

Case 1:	$U_g=-5$ m·s^{-1}, $V_{max}=20$ m·s^{-1}, zero gradient b. c. for u and v, radiation b. c. for θ, moisture profile RH_1.
Case 1B:	$U_g=-5$ m·s^{-1}, $V_{max}=20$ m·s^{-1}, radiation b. c. for u and v, zero gradient b. c. for θ, moisture profile RH_1.
Case 1G:	$U_g=-5$ m·s^{-1}, $V_{max}=20$ m·s^{-1}, radiation b. c. for u and v, zero gradient b. c. for θ, moisture profile RH_1. non-separated pressure treatment.
Case 1F:	$U_g=-10$ m·s^{-1}, $V_{max}=20$ m·s^{-1}, zero gradient b. c. for u and v, radiation b. c. for θ, moisture profile RH_1,
Case 2:	$U_g=-5$ m·s^{-1}, $V_{max}=40$ m·s^{-1}, zero gradient b. c. for u and v, radiation b. c. for θ, moisture profile RH_2.

STREAMLINE
(Z=50 M,HR=00)
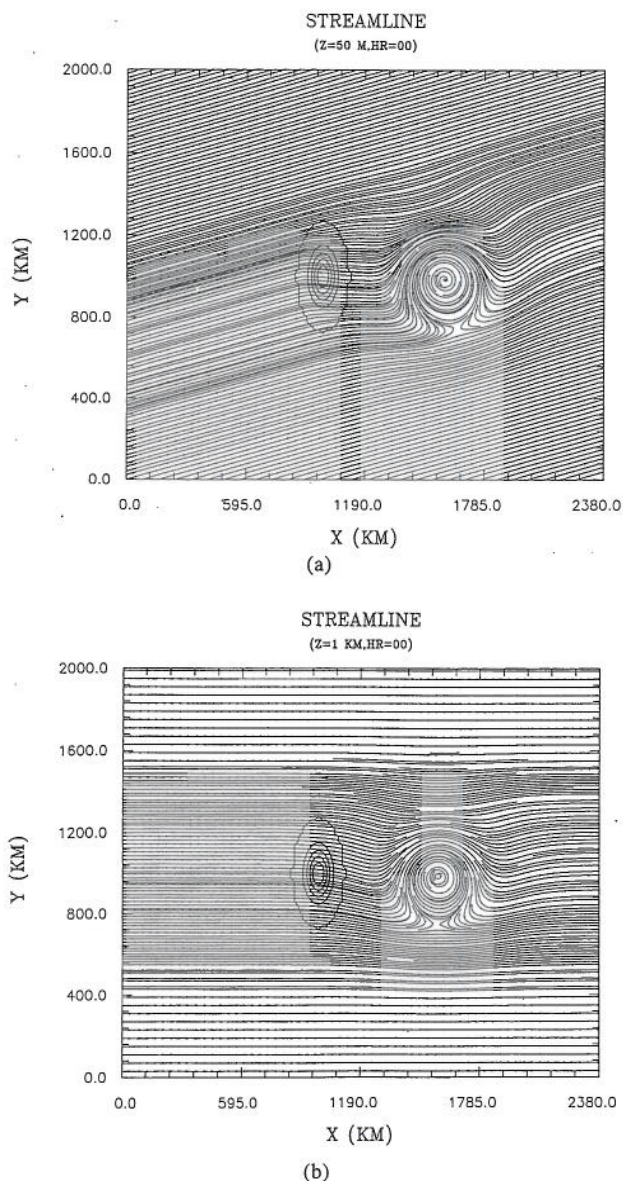

(a)

STREAMLINE
(Z=1 KM,HR=00)

(b)

Fig. 2. The initial fields for Case 1 (weaker typhoon). (a) Stream-lines at 50 m above the surface, (b) streamlines at 1 km above the surface. The topography height is plotted using bold lines with a contour interval of 500 m. The outermost bold line represents the coastline.

PRESSURE PERTURBATION
(Z=0 M,HR=00)

CONTOUR FROM −2.4000   TO 0.00000E+00 INTERVAL OF 0.10000

(a)
U
(Z=3 KM,HR=00)

CONTOUR FROM −22.000   TO 12.000   INTERVAL OF 2.0000

(b)

Fig. 3. The initial fields for Case 1 (weaker typhoon). (a) Pressure perturbation at the surface with a contour interval of 0.1 mb, (b) the east-west wind component (u) at 3 km above the surface with a contour interval of 2.0 m·s^{-1}.

For simplicity, the sea surface temperature was assumed to be constant with the model integration time while a neutral surface layer was assumed over the ground. The surface roughness used in the PBL closure was prescribed as a constant of 4 cm. There were no diurnal effects or radiation processes in this study.

Since it was rather difficult to initialize the model with a prescribed non-homogeneous flow, the vertical profiles of the potential temperature and moisture for the vortex were also used for the ambient conditions in this study. Hence, the moisture profile of the water
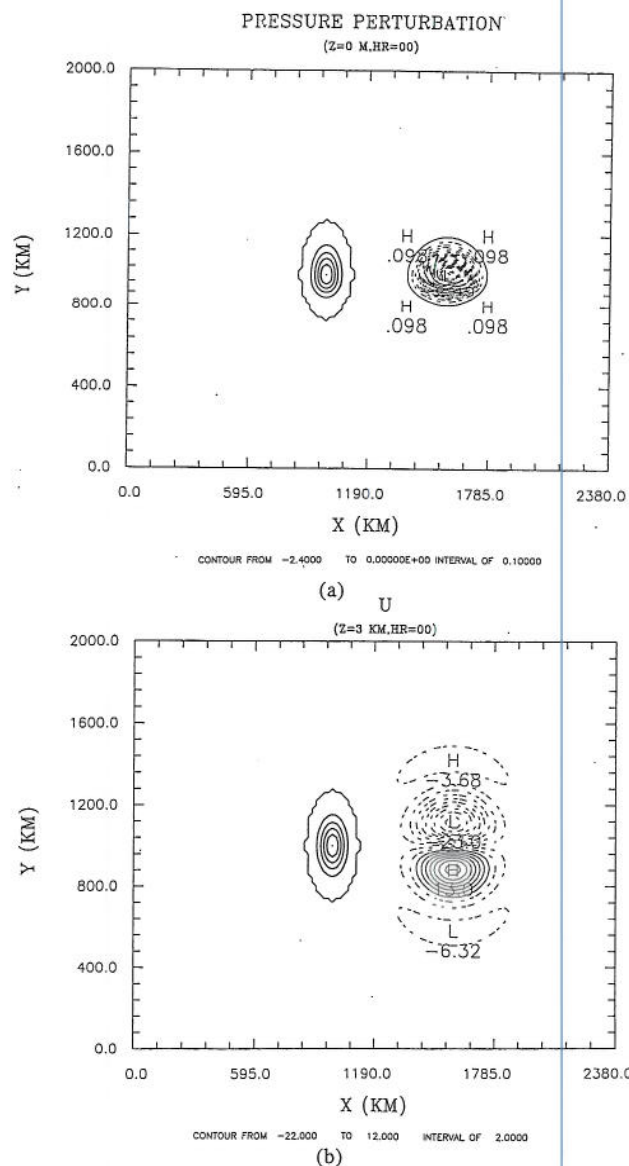
vapor RH$_1$ enabled the ambient environment to supply high moisture content for vortex intensification. The near-surface unstable flow over the ocean, typical of conditions for hurricane development, however, became neutral over the ground with an assumed zero vertical heat flux.

1. Weaker Vortex

The weaker vortex had a maximum tangential wind of 20 m·s^{-1}. Case 1 was the control run with an environmental easterly wind of 5 m·s^{-1}. Figure 2

shows the superimposed streamlines of the vortex circulation and the environmental flow, the former in gradient-wind balance and the latter in Ekman wind balance. Both flows were non-divergent; hence, their superimposition was also non-divergent. Due to the boundary-layer frictional effects, the near-surface easterly flow became east-northeasterly across the isobars and toward the low. Note that the entire horizontal plane shown in this study is on the surface of constant σ; hence, the real streamlines may not be closely indicated. The associated pressure perturbation at the surface is shown in Fig. 3(a). A negative value of -2.4 mb was produced at the vortex center. The east-west wind component above the boundary layer was

nearly symmetric about the vortex center, with negative values to the north and positive values to the south (Fig. 3(b)). Due to the existence of the steering flow, the maximum wind speed was present to the north of the vortex center. The vortex circulation moved westward at 12 h (integration time), with a near-surface flow spiraling into its center (Fig. 4(a)). The large angle of the streamlines incident to the isobars reflects the effective mass pumping through the turbulent mixture. At this time, the topographical circulation, e.g., the leeside vortex, was induced (Fig. 4). Since we are more interested in the track evolution, the processes of the cloud bands in the vortex circulation are not shown here, but they can be found in Huang
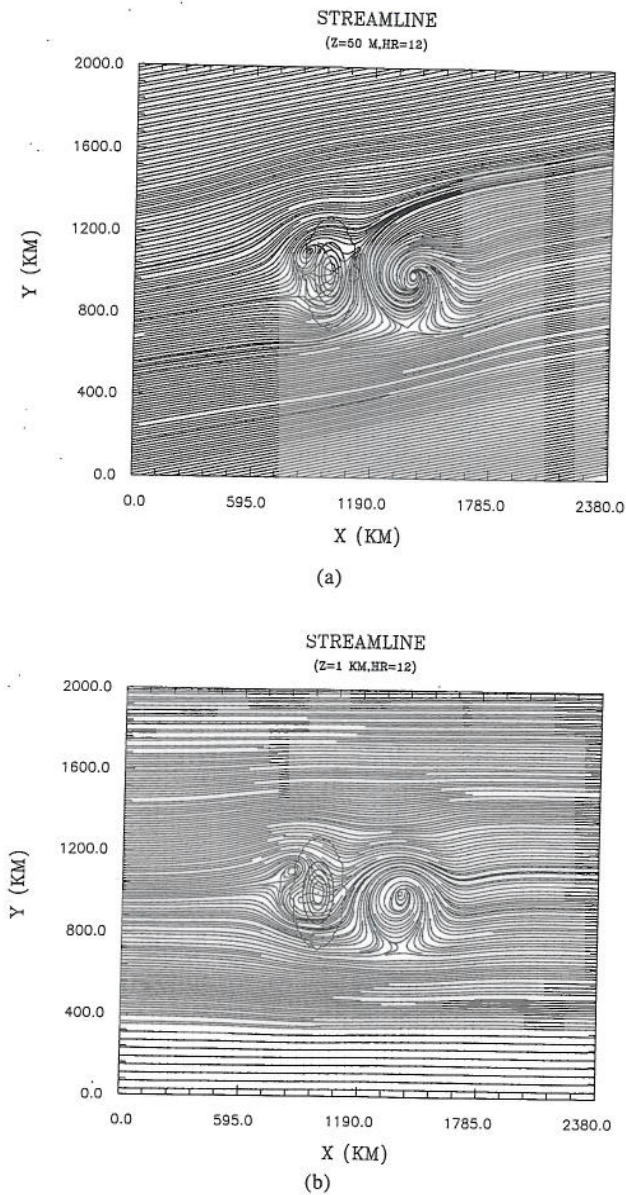

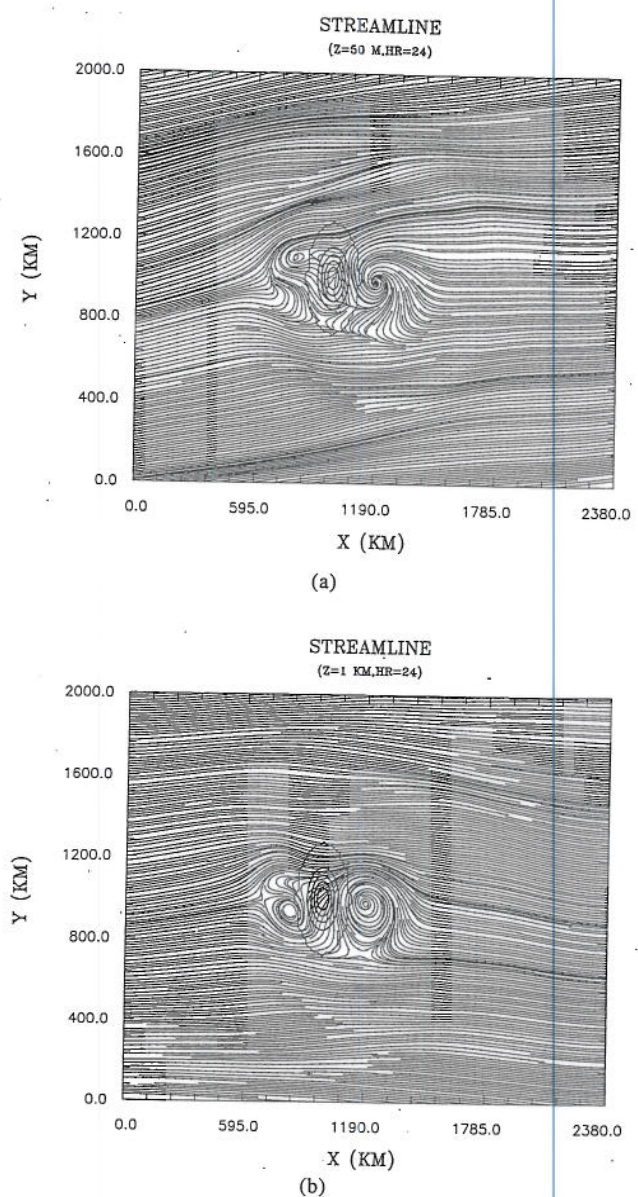
Fig. 4. As in Fig. 2 but at 12 h.

Fig. 5. As in Fig. 2 but at 24 h.

(1993).

At 24 h, the vortex center was approaching land but, its position at all vertical levels remained at about the same latitude. This result of an almost straight track is quite interesting since the near-surface flow somewhat pointed to the south, as shown in Fig. 5. Comparing Figs. 4 and 5, one can find that the low-level vortex shrank somewhat as it approached the island. Also, the lee vortex moved further offshore due possibly to the changed angle of the impinging flow. As a consequence, the associated low center intensified to -4.6 mb (not shown).

The vortex center made landfall by 30 h but had been deflected to the south of its original latitude as shown in Fig. 6. The outer vortex circulation surrounded the whole island and appeared to dominate the lee vortices since they were no longer supported by an upstream straight flow. Indeed, a secondary low was produced at the leeside of the island and will be discussed in the next section. The low-level vortex had further shrunk in size as the center approached closer to the topography. The vortex center passed around the southern ring of the steep slope and reached the southwestern side of the mountain peak at 36 h, with a well aligned low-level structure as shown in Fig. 7.

The vortex center migrated to its initial latitude at 42 h and then overshot slightly northward at 48 h as shown in Figs. 8 and 9, respectively. The center
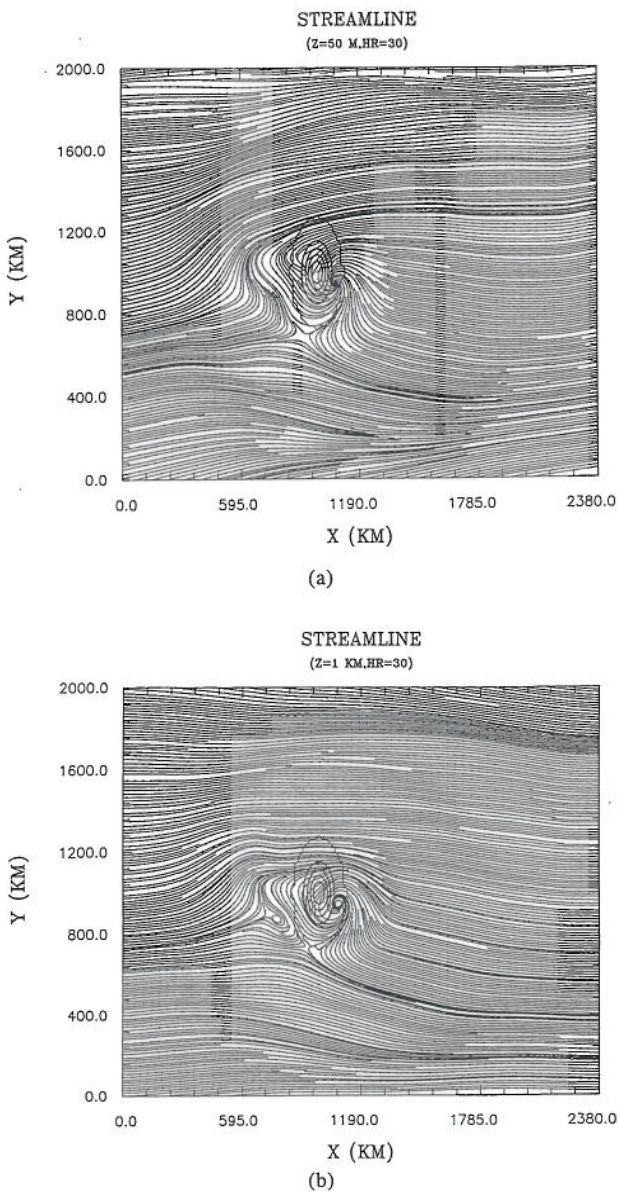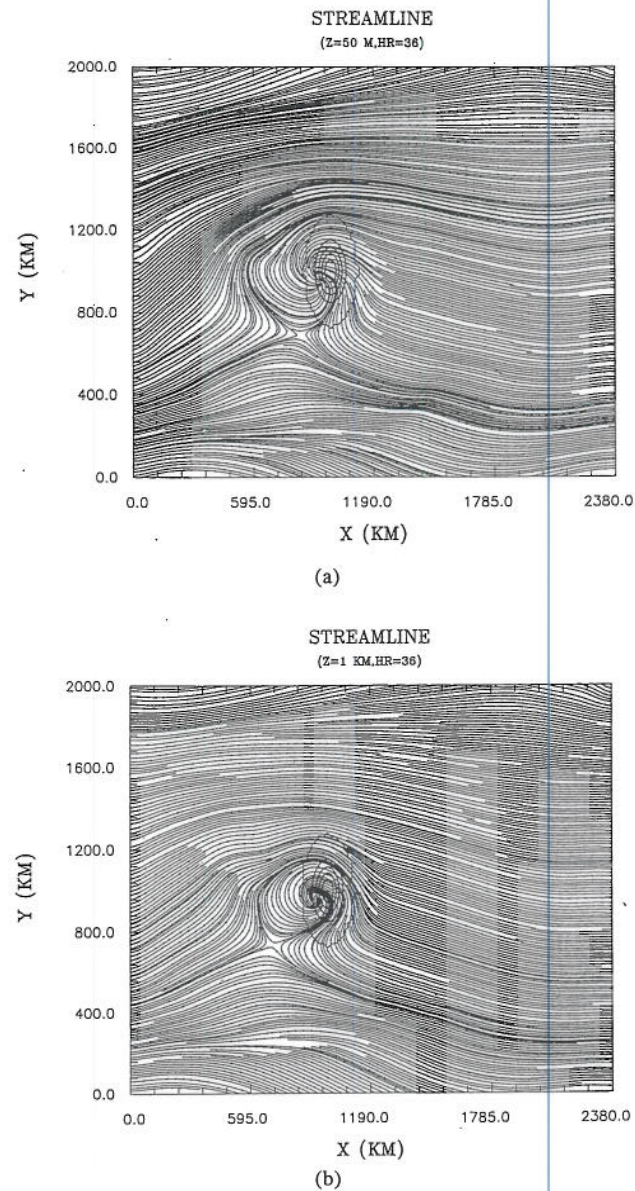

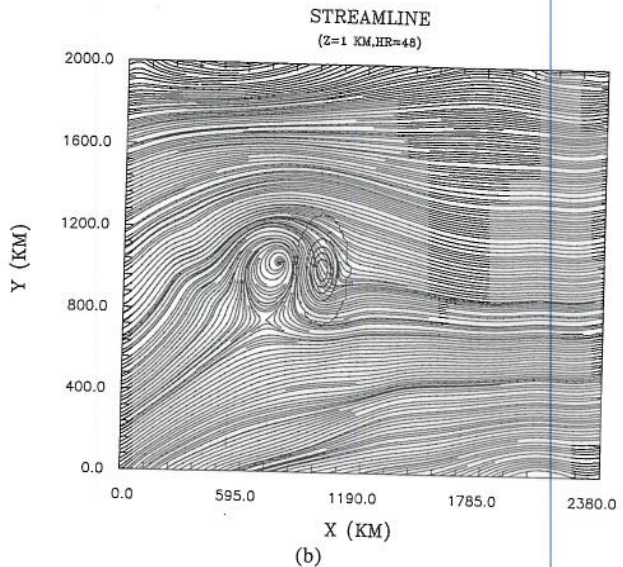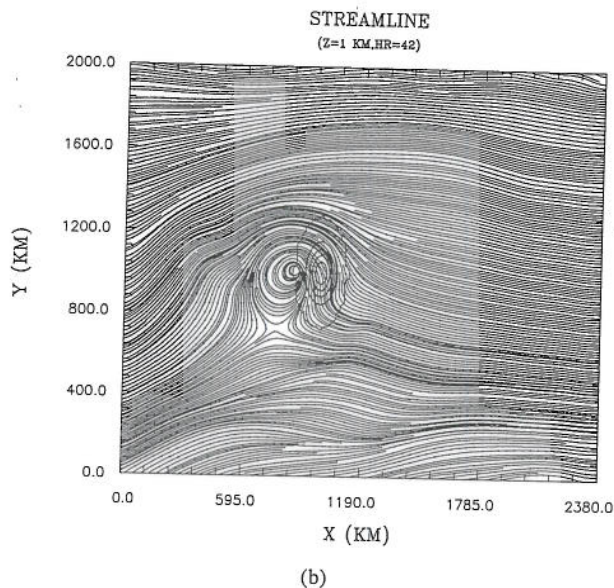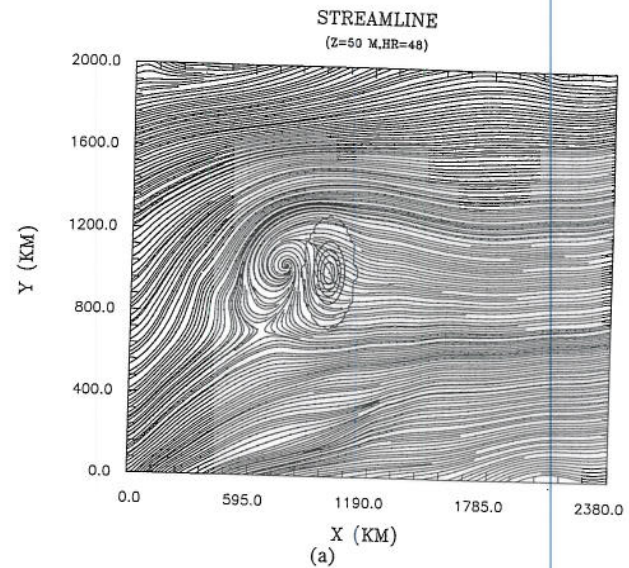Fig. 6. As in Fig. 2 but at 30 h.

Fig. 7. As in Fig. 2 but at 36 h.

STREAMLINE
(Z=50 M,HR=42)

(a)

STREAMLINE
(Z=50 M,HR=48)

(a)

STREAMLINE
(Z=1 KM,HR=42)

(b)

Fig. 8. As in Fig. 2 but at 42 h.

STREAMLINE
(Z=1 KM,HR=48)
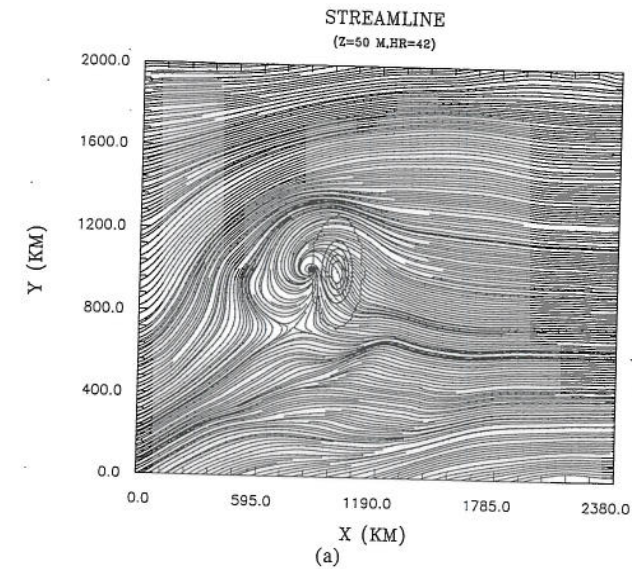

(b)

Fig. 9. As in Fig. 2 but at 48 h.

then remained situated at the same latitude before the end of the simulation time of 60 h (not shown). Hence, it appears that the northward movement of the center by leaving time may have been due to the strong southerly flow to the east, but as a result, this tendency was quickly offset by the south-westward flow to the west of the center after leaving.

Since one goal of this study was to show the performance of typhoon initialization, a vertical cross-section of the potential temperature at $J=51$ (cutting through the central peak) is shown in Fig. 10. At the initial time, a rather warm core was produced at the middle-level vortex center. As previously mentioned, this warm core was present in response to the hydro-

static balance without the inward (to the center) vertical motion. Due to this weak vortex, an initial non-divergent gradient-wind approximation seems to be feasible. The warm core was quickly modified during the integration time. As can be seen in this figure, the vortex deepened and overshot greatly. The modeled vortex structure was similar to that observed hurricanes discussed in Anthes (1982). Indeed, the vortex intensity did not vary very much before hitting the terrain.

For this weaker steering flow, the associated lateral boundary conditions were tested. When the Orlanski radiation condition was applied for the momentum and thermodynamic variables in the simulation, it was found that abnormal disturbances were produced near the
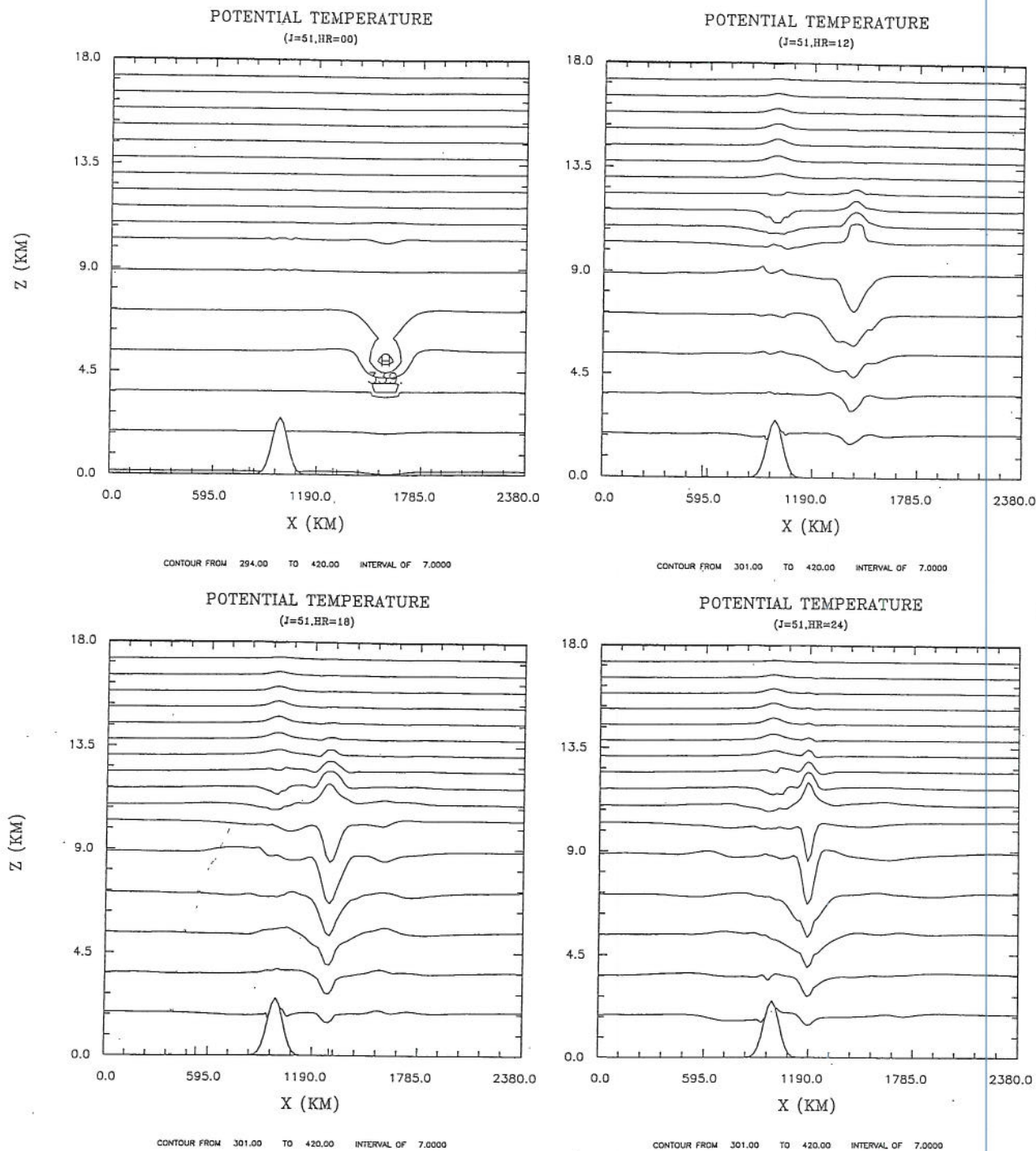
POTENTIAL TEMPERATURE
(J=51,HR=00)

POTENTIAL TEMPERATURE
(J=51,HR=12)

CONTOUR FROM   294.00   TO   420.00   INTERVAL OF   7.0000

CONTOUR FROM   301.00   TO   420.00   INTERVAL OF   7.0000

POTENTIAL TEMPERATURE
(J=51,HR=18)

POTENTIAL TEMPERATURE
(J=51,HR=24)

CONTOUR FROM   301.00   TO   420.00   INTERVAL OF   7.0000

CONTOUR FROM   301.00   TO   420.00   INTERVAL OF   7.0000

Fig. 10. The x-z cross-section results of the potential temperature with J=51 (cutting through the mountain peak) for Case 1 (weaker typhoon) at different times of 0, 12, 18, and 24 h. Contour interval is 7 K.

upstream boundary as the vortex hit the terrain (not shown). The abnormal disturbances may have been caused by our imperfect numerical schemes. However, the radiation boundary condition was successfully applied to 2-D simulations of strong mountain waves with little distortion (not shown). The result may be explained by the fact that the inflow was well defined for the 2-D flow so that both the phase speed and direction were easier to determine. For 3-D simulations, the inflow may vary with time and the associated phase speed may be inaccurately estimated, particularly near the weak flow zone as in the northern and

southern boundaries for our cases. To avoid this problem, it might be better to allow no horizontal gradient of the predicted variables at the boundary or to use a larger model domain.

The reason why the lateral boundary condition was tested appears to be important since our research was rather limited to current computer efficiency. Before the advent of a perfect lateral boundary condition, we should compromise to use a more economical scheme. As described in Table 1, Case 1B exchanged the boundary conditions for wind and potential temperature. Figure 11 shows the results of Case 1B at 60 h. As can be seen, the lateral flow at 60 h was still less wavy as compared to that at 48 h for Case

1. However, the positions of the vortex centers and the circulations for the two cases were very similar. Hence, we conclude that the imperfection of our boundary conditions did not play a crucial role in determining the track.

Another interesting case (Case 1F) examined whether the track deflection was different if the same conditions were retained except for the steering wind speed, which was doubled. The doubled steering wind speed resulted in a doubled vortex translational speed (10 m·s^{-1}) prior to landfall. Figure 12 shows the simulation results for Case 1F at 12 h. It is quite clear in this figure that the vortex was slightly deflected to the
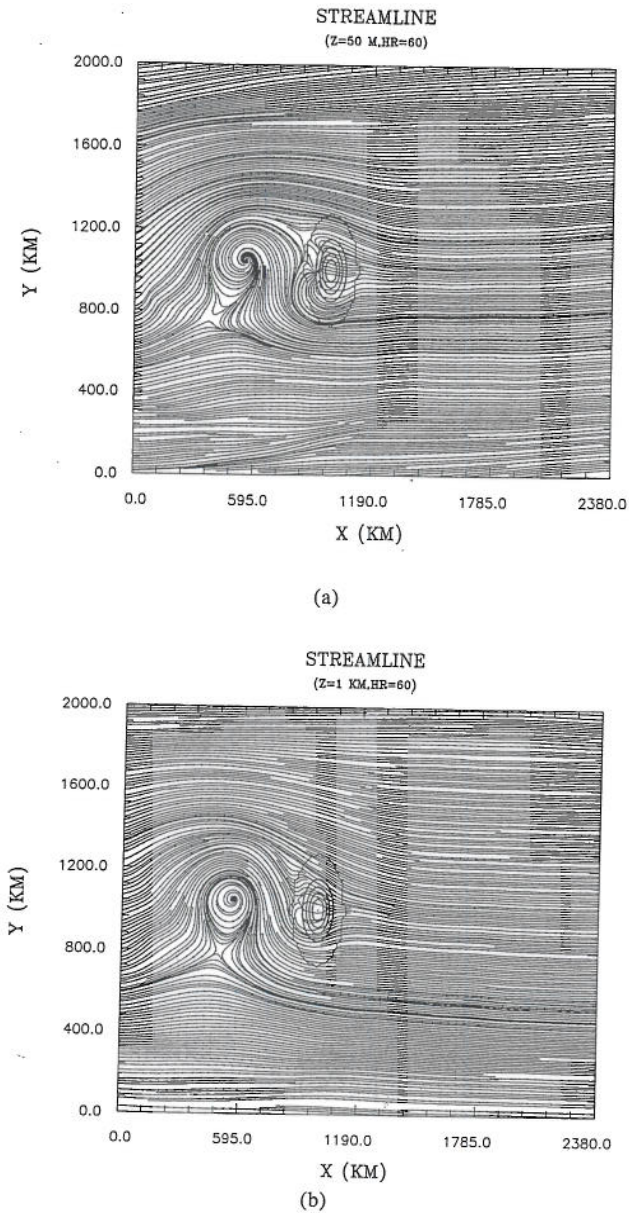
STREAMLINE
(Z=50 M,HR=60)

(a)

STREAMLINE
(Z=50 M,HR=12)

(a)

STREAMLINE
(Z=1 KM,HR=60)

(b)

Fig. 11. As in Fig. 2 but at 60 h for Case 1B (weaker typhoon).
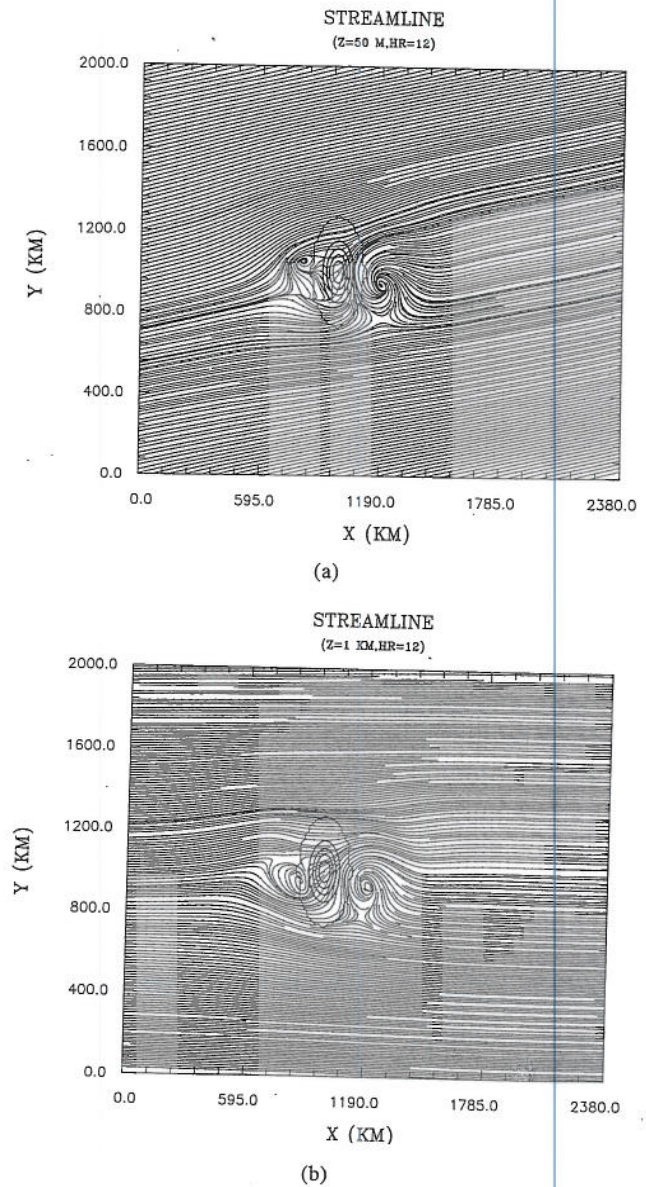
STREAMLINE
(Z=1 KM,HR=12)

(b)

Fig. 12. As in Fig. 2 but at 12 h for Case 1F (weaker and faster typhoon).

south at this time and the deflection was further southward than that at 24 h for Case 1 (Fig. 5), but that both vortex centers for the two cases advected by about the same distance. This seems to show that the translational speed of the vortex was completely dominated by the ambient wind in the absence of β-effects. The vortex center indeed experienced a similar track for Cases 1 and 1F. The results at 24 h for Case 1F are shown in Fig. 13. Compared to Fig. 9, both vortex centers are quite close in position.

2. Stronger Vortex

Case 2 employed the same conditions of Case 1 except that the maximum tangential wind speed was doubled to 40 m·s^{-1}, and a dryer moisture profile (RH$_2$) was used. As mentioned before, we have attempted to use the more moist RH$_1$ profile, but this resulted in an unreasonably strong and larger vortex that appeared to be not well balanced by internal nonlinear dissipation. Observationally, stronger typhoons are frequently associated with larger sizes. However, the typhoon circulated close to the upstream boundary when the radius of its maximum tangential wind was doubled in our cases, which employed a horizontal resolution of 20 km. In this study, the typhoon size thus was fixed for all the cases.
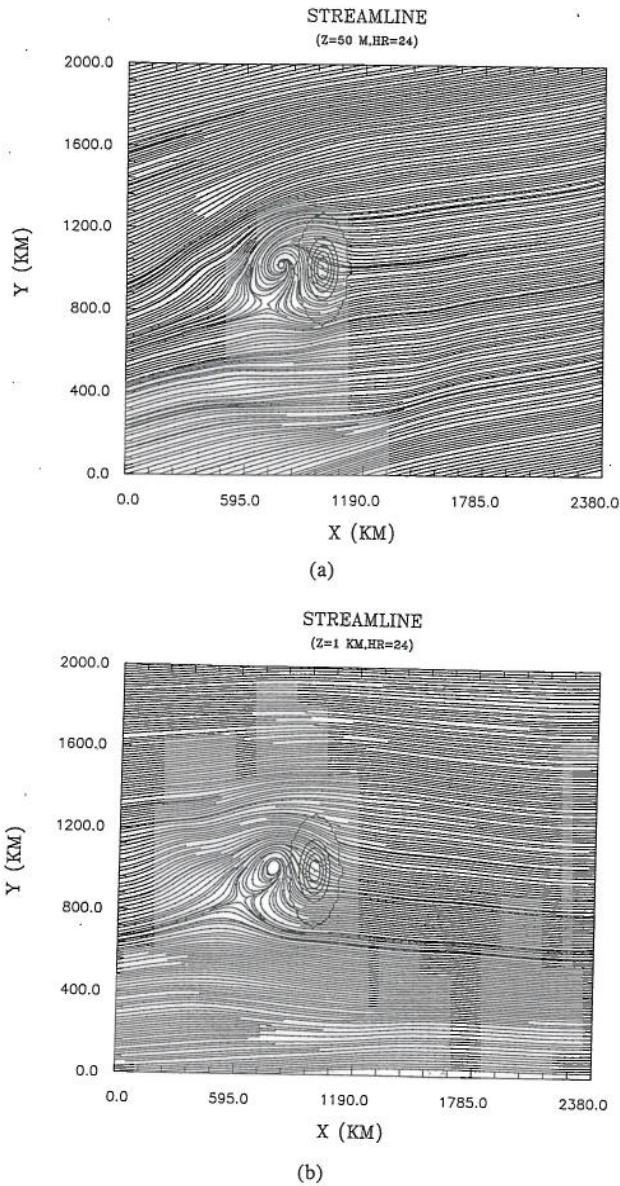
The stronger vortex exhibited a much wider cir-

(a)

(b)

Fig. 13. As in Fig. 2 but at 24 h for Case 1F (weaker and faster typhoon).
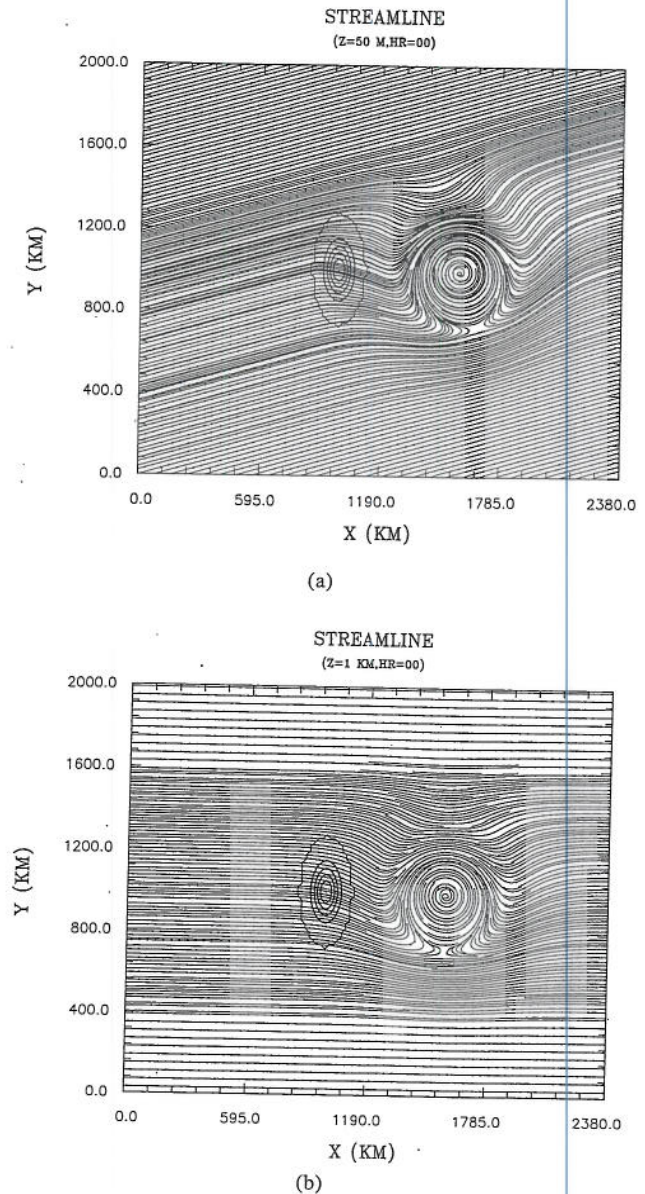

(a)

(b)

Fig. 14. As in Fig. 2 but for Case 2 (stronger typhoon).

culation obtained from the initialization scheme as shown in Fig. 14. The pressure perturbation induced at the vortex center also increased to -8.5 mb. The increase in the size of the induced vortex resulted from the gradient-wind balance, in which a larger distance was required for the pressure gradient to decay in response to the doubled maximum tangential wind speed. Close examination of this figure also reveals that there was a deflection region of the steering flow as it was superimposed on the vortex circulation. Note that both the frictional near-surface flow and the initial inviscid vortex circulation were non-divergent. This initialized vortex structure is somewhat unrealistic for observed typhoons but appears to be feasible since it does not

result in abnormal development at later times. For example, the vortex flow at 12 h became a spiral with a smooth transitional steering flow, which is more consistence with real typhoons (Fig. 15). Since the steering flow was the same as in Case 1, lee vortices were also present in this case.

To illustrate the difficulty of initializing a strong vortex, a vertical cross-section of potential temperature
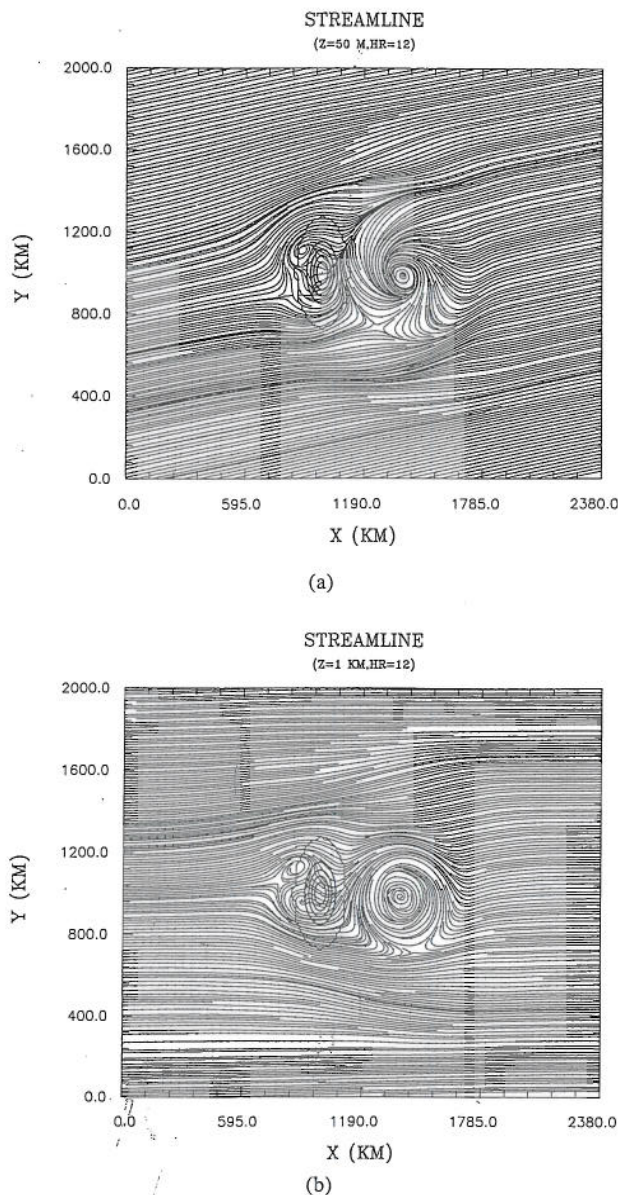
STREAMLINE
(Z=50 M,HR=12)

(a)

STREAMLINE
(Z=1 KM,HR=12)

(b)

Fig. 15. As in Fig. 2 but at 12 h for Case 2 (stronger typhoon).

POTENTIAL TEMPERATURE
(J=51,HR=00)

CONTOUR FROM 294.00 TO 420.00 INTERVAL OF 7.0000

POTENTIAL TEMPERATURE
(J=51,HR=12)

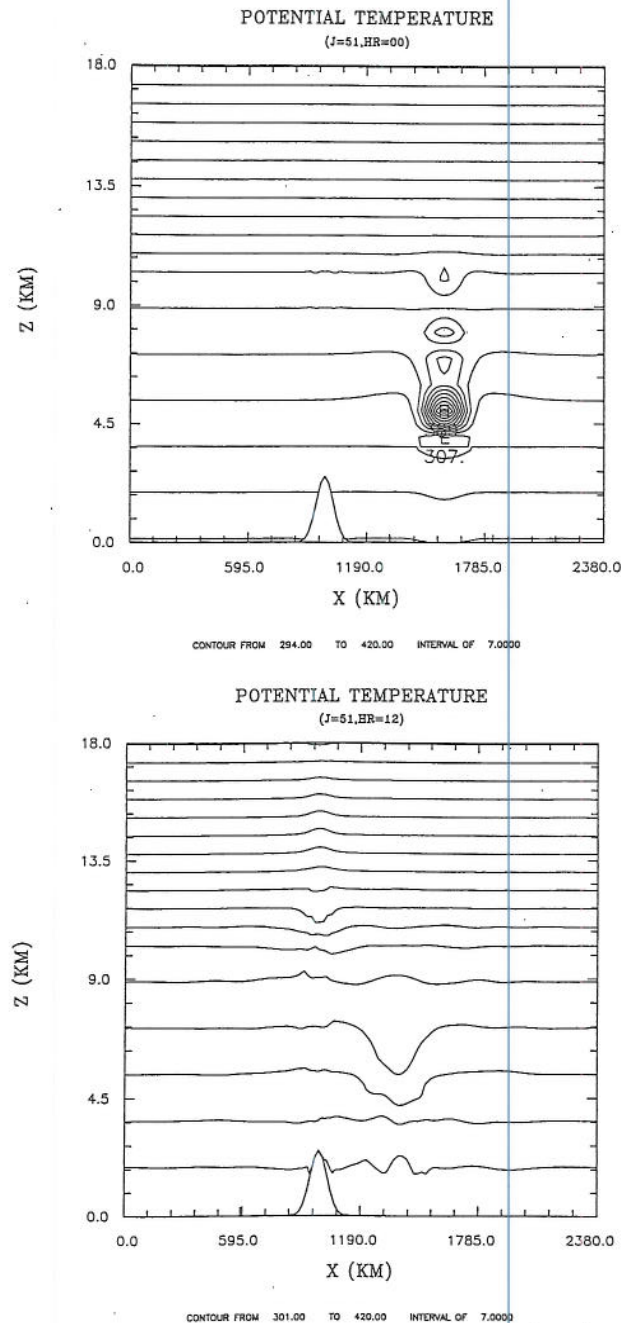CONTOUR FROM 301.00 TO 420.00 INTERVAL OF 7.0000

Fig. 16. The x-z cross-section results of the potential temperature with J=51 (cutting through the mountain peak) for Case 2 (stronger typhoon) at different times of 0 h and 12 h. Contour interval is 7 K.

at J=51 is shown in Fig. 16. As can be seen, an extraordinary super warm core was generated at the mid-levels of the vortex center. This warm core in the region of maximum vertical shear of the tangential wind was present due to the hydrostatic balance when the pressure perturbation was determined by the horizontal distribution of the tangential wind. The abnormal vortex structure was quickly modified during the time integration when the full model physics were involved. At 12 h, the extremely warm core had been completely neutralized. The warm center region was wider and deeper than that for the weaker case (Fig. 10). As seen in Fig. 15, the low-level vortex after adjustment was similar in shape and size to the weaker one. It is not clear at this point whether the similar adjustment solely resulted from the same radius of the maximum tangential wind. This issue should be further investigated in the future.

Although there were some deviations between the stronger and weaker vortices, they exhibited similar tracks when they reached land. Prior to landfall, the positions of both vortex centers were very similar (not shown). Figure 17 shows the results for Case 2 at 30 h. As can be seen, the vortex center deflected slightly to the south, very similar to Case 1 (see Fig. 6). The warm-center structures for the two cases were also similar by the time (not shown). Since the stronger vortex circulation was similar to the weaker one, the former track was also similar to the latter after landfall as shown before.

IV. Discussions

1. Vortex Tracks

Past numerical studies using symmetric topography (as in this study) have obtained valuable findings for westbound typhoons. Chang (1982) and Yeh and Elsberry (1993a, 1993b) found that the vortex centers tended to be deflected northward as an easterly typhoon translated toward the northern or central part of an idealized topography. Bender *et al.* (1987), in simulations with a realistic Taiwan topography in the β-plane, also found an upstream northward deflection and suggested that it correlated with the increase in the southerly wind component of the low-level average inner vortex. However, our simulation results indicate that a southward deflection could also exist for the same problem. A close check of the simulation parameters reveals that the mountain sizes in Chang (1982) and Yeh and Elsberry (1993a, 1993b) were nearly double those in this study, and that the implanted vortex was also larger. Furthermore, the horizontal resolutions of 60 km for Chang (1982) and 45 km for Yeh and

STREAMLINE
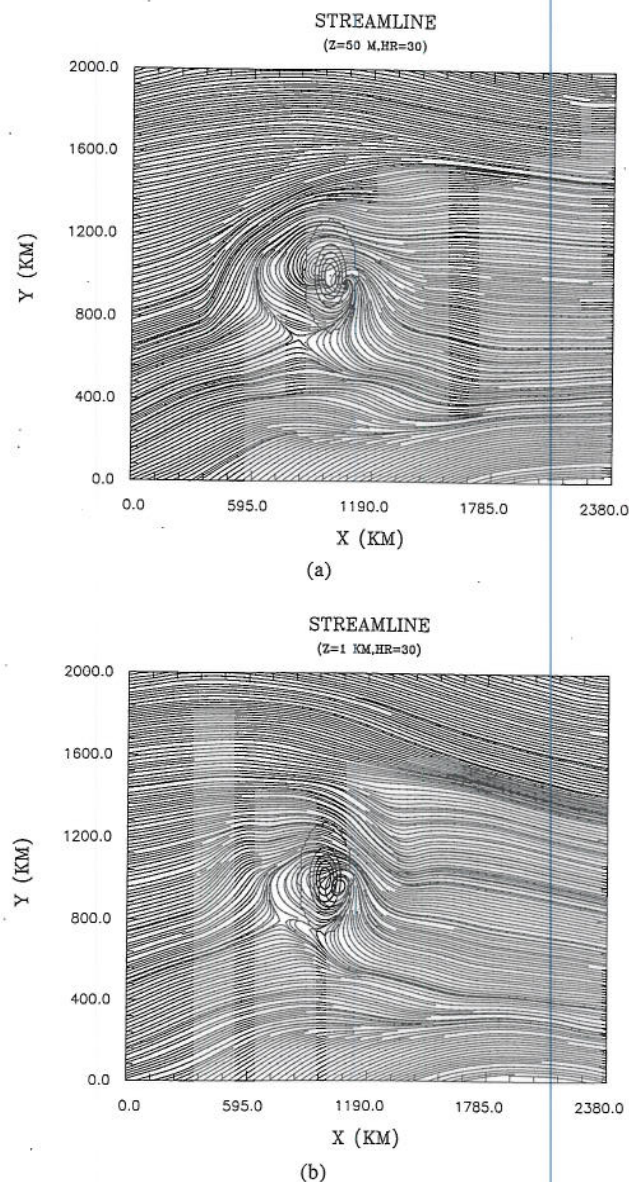(Z=50 M,HR=30)

STREAMLINE
(Z=1 KM,HR=30)

Fig. 17. As in Fig. 2 but at 30 h for Case 2 (stronger typhoon).

Elsberry (1993a, 1993b) are much larger than 20 km used in this study. The effects of this resolution difference need to be investigated.

To understand the sensitivity of the track deflection to steering flow variation, another numerical test (Case 1G) was conducted. In this case, the pressure was not separated into geostrophic and non-geostrophic parts, the former being kept unchanged with time in the previous cases. The advantage of the non-separated pressure treatment was simplicity of modeling, but this could introduce some variation of the steering flow as exhibited in Fig. 18. As can be seen, the low-level center in this case deflected slightly to the north at 24 h. Indeed, the steering flow turned somewhat
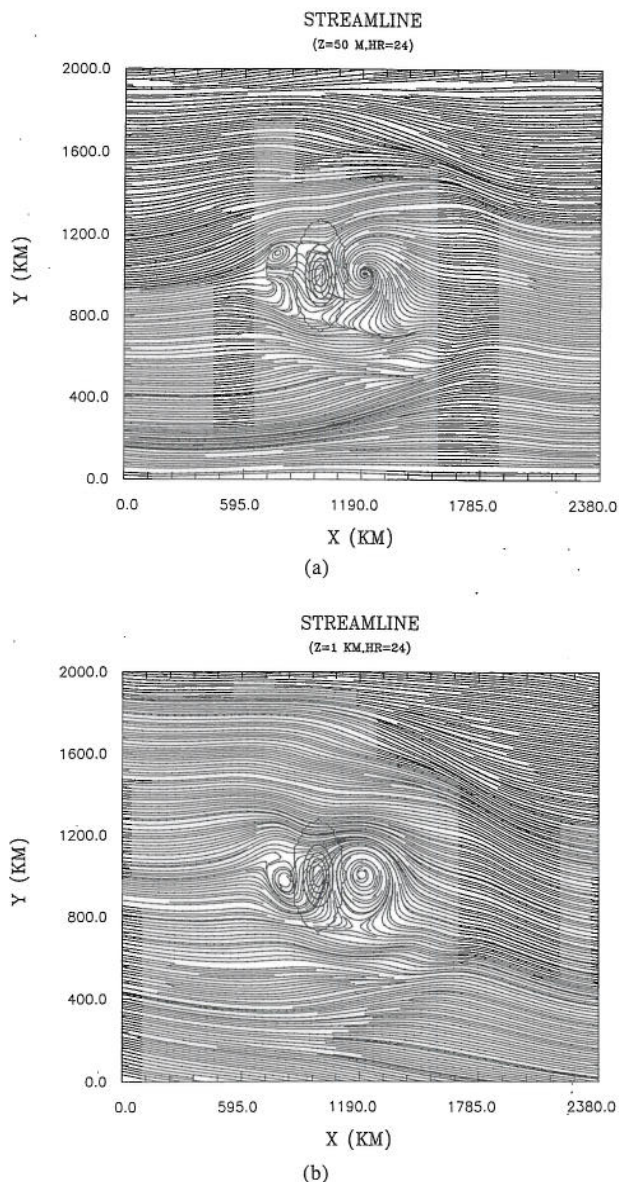
STREAMLINE
(Z=50 M,HR=24)

(a)

STREAMLINE
(Z=1 KM,HR=24)

(b)

Fig. 18. As in Fig. 2 but at 24 h for Case 1G (weaker typhoon).

northward and was probably responsible for the northward track deflection prior to landfall. Note that the initial flow was completely easterly; thus, the upstream flow deflection was entirely due to the adjustment in the thermal wind approximation.

We have found that it is difficult to maintain a long-term non-deflected flow if the initial geostrophic wind is not retained intact. Although the total wind above the PBL should remain geostrophic if no mesoscale force is involved, the thermal wind balance tested is not completely satisfied in the initialization with a prescribed homogeneous temperature field. Assuming a perfect thermal wind balance initially, the geostrophic part from the non-separated treatment of

the pressure may also be affected by gravity waves propagating upstream. This would require a much larger upstream domain in the vortex-terrain interaction cases. The split geostrophic part is not modified by the mesoscale effects; thus, the upstream steering flow structure can be kept intact. With no significantly disturbed upstream flow, the treatments should produce similar results since Coriolis forcing is not dominant in the mesoscale topographic region. As expected, both Cases 1G and 1 exhibited similar flow patterns as their vortices approached the island although, in the former case, the upstream flow turned slightly. At later times, the track for Case 1G also turned southward similar to that for Case 1 (not shown).

The far upstream track deflection was also present in the numerical simulations of easterly drifting vortices carried out by Chang (1982) and Yeh and Elsberry (1993a). Their deflection angle was about 5 degrees to the north, which is nearly equal to that in our Case 1G. Indeed, the track deviation from the ambient wind direction was also present in the only-ocean control run of Yeh and Elsberry (1993a) in the absence of β-effects. Hence, the far upstream track deflection is not related to either terrain effects or β-effects. Here, we have reported on the sensitivity of the vortex movement to geostrophic wind variation as evident in the results for Case 1G where southward deflection after the landfall was present in spite of the northward deflected steering flow.

The track deflections for different cases have been explained in the previous section. For Case 1, the positions of the vortex center at a 1 km height determined by maximum vorticity were (80, 51) at 0 h, (74, 50) at 6 h, (71, 52) at 12 h, (65, 50) at 18 h, (60, 50) at 24 h, and (55, 49) at 30 h. The southward track deflection during landfall could be clearly seen in the vorticity field. Figure 19 summarizes the tracks of the vortex center at near-surface and at a 3 km height for Case 1; here, the vortex center is defined as the circulation center, which is rather subjective, during the landfall time. As can be seen, there was a small departure of the center position from the original latitude during the adjustment period as the vortex was introduced; however, the vortex center in general moved straight ahead in response to the easterly ambient flow. The southward deflection of the vortex center was detected at a near-surface height and at a 3 km height just prior to landfall (at 27 h). During the track deflection time, the movement of the near-surface vortex center appeared to be slowed down, but only slightly. The vortex center tended to pass around the mountain peak and to then move northward as it left the island, exhibiting a considerably faster translational speed as can be seen from the larger spacing
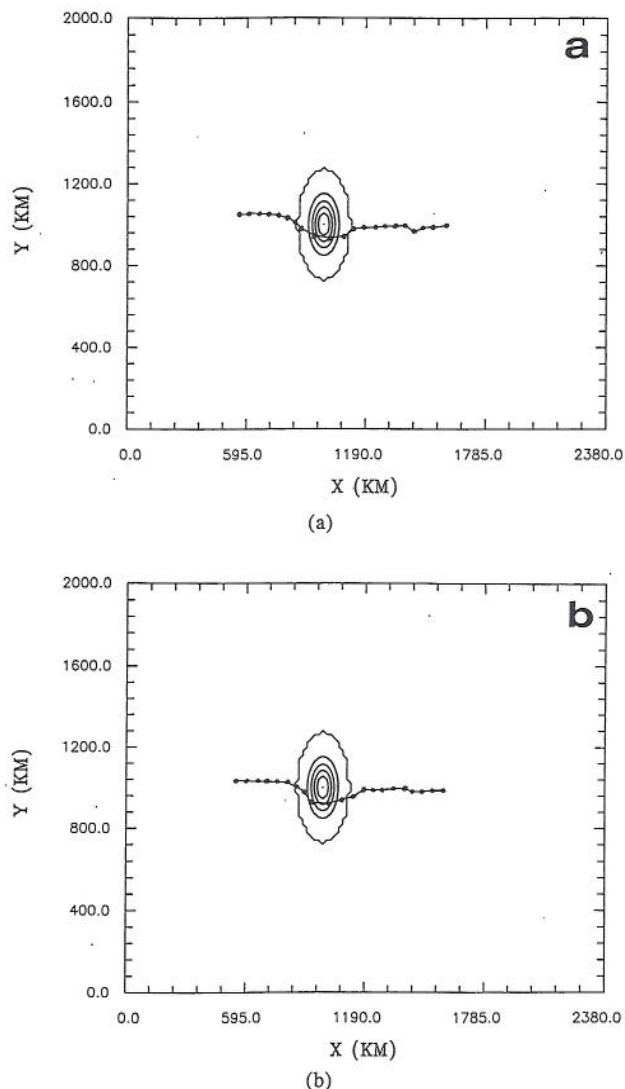
(a)

(b)

Fig. 19. The positions of the vortex center every 3 h for Case 1 (a) at a 50 m height; (b) at a 3 km height. The vortex center is defined as the circulation center positioned by a subjective judgment.

(a)

(b)

Fig. 20. The vertical profiles of the average v-momentum budgets in the vicinity of the vortex center at 12 h. (a) at the vortex core, (b) in the square region of 5×5 grid points centered on the vortex core. The symbols used are A: advection terms, B: boundary layer vertical diffusion, C: Coriolis forcing, G: geostrophic forcing, N: nonlinear horizontal diffusion, P: ageostrophic pressure gradient, and T: the total net forcing.

of the tracking points over the island in Fig. 19. During the offshore time, the vortex center translated straight westward.

2. Vortex Dynamics

To understand the relative importance of the dynamical forces and their roles in track deflection, the budgets of the momentum equations were analyzed in this study. The v-momentum budgets at the vortex center (71, 52) at 12 h are shown in Fig. 20. To inspect the sensitivity of the tiny core, the average forcing of 5×5 grid points (NG=2, 2 expanded grids on both sides of the x- and y-directions) in the square-area ce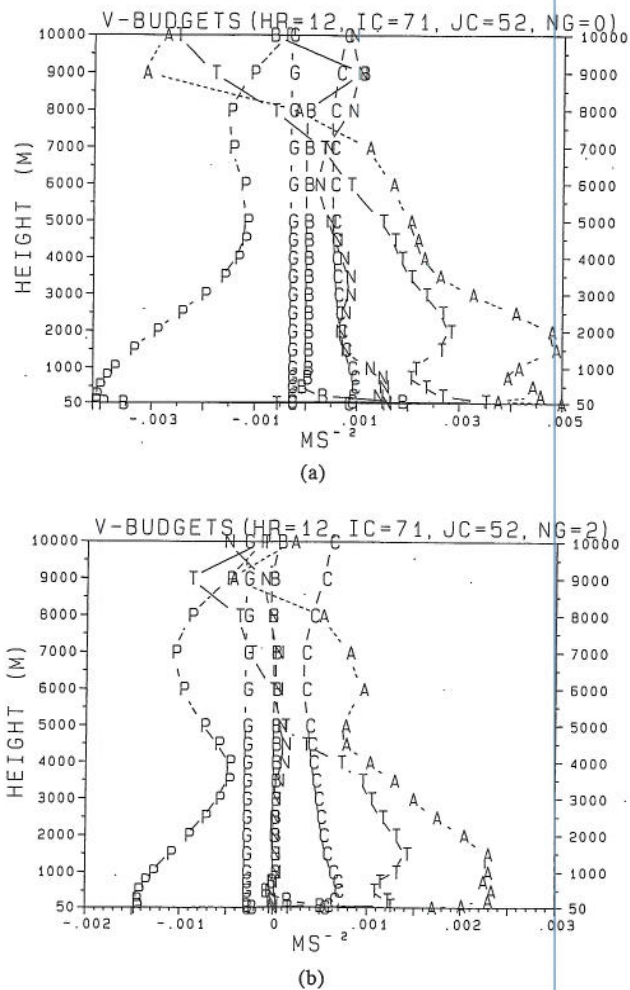ntered at the vortex center is also shown in this figure. As can be seen from the v-momentum budgets at the vortex center, the advection term (denoted as A) was offset primarily by the ageostrophic pressure gradient (marked by P) in the maritime vortex core, in which the Coriolis force (marked by C) and geostrophic pressure gradient (marked by G) were secondary. The nonlinear horizontal diffusion (marked by N) was also unimportant. As a result, there was net northward (southward) acceleration (marked by T) at low (high) levels, indicating that the wind acceleration on average was not symmetric. The vortex, viewed as a whole, tended to move northward if the wind acceleration at low levels played a steering role. However, the vortex at this time was not pushed to the north of the original latitude.
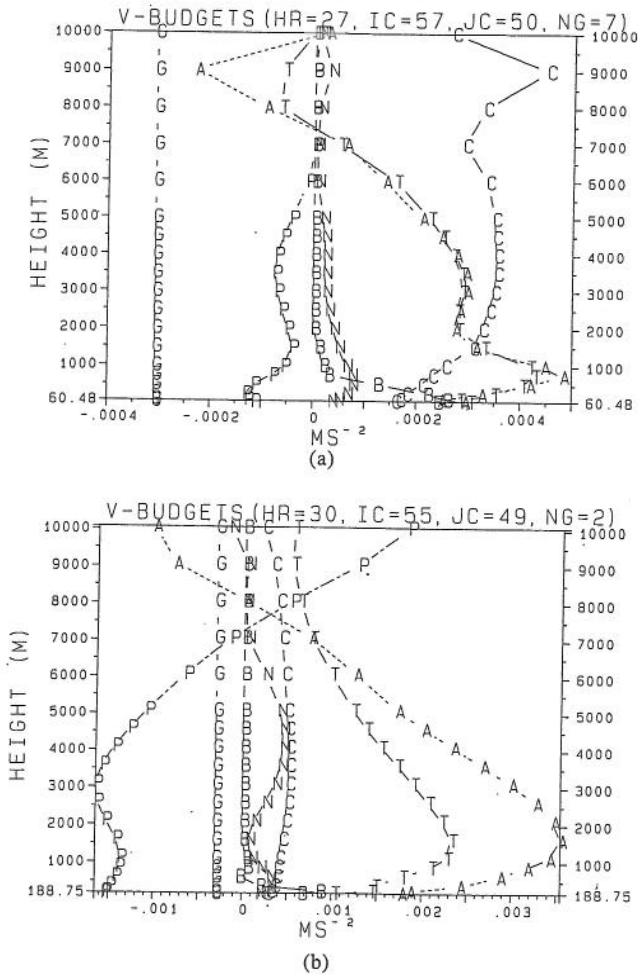
Fig. 21. As in Fig. 20 but for the square regions of (a) 15 × 15 grid points at 27 h and (b) 5 × 5 grid points at 30 h. The symbols used are the same as those in Fig. 20.

The primary balance between the advection and the ageostrophic pressure gradient in the core region was also evident at 27 h and 30 h when the track began to deflect southward. As the average square-area was increased to 15×15 grid points (NG=7) centered at the vortex center, the importance of the Coriolis force and ambient geostrophic forcing became apparent as shown in Fig. 21; the forcings together with the advection dominated the flow at upper levels, indicating a good approximation of the gradient-wind balance. A close look reveals that the net average forcing was well represented by the advection term. This indicates that the average vortex circulation did not accelerate northward or southward in a Lagrangian view. The boundary layer forcing (marked by B) was important only at lower levels while exhibiting northward acceleration. Hence, no southward movement could be inferred if the vortex center primarily responsed to the inner core dynamics or average forcing of its adjacent area. The

vortex center, however, exhibited a southward movement just prior to landfall. A remarkable tendency shown by the budgets in Figs. 20 and 21 was the southward ageostrophic forcing. Indeed, only the ageostrophic forcing showed a strong southward tendency of the flow. For uniform small-Froude number mesoscale flow over meso-β scale topography, the upstream flow of the mountain will be deflected more southward than northward in the presence of the Coriolis force (Smith, 1979).

The deceleration of the vortex movement at the beginning of its deflection can be explained in terms of the u-momentum budgets as shown in Fig. 22. As can be seen, the inner core region (NG=2) at lower levels at 30 h was dominated by the ageostrophic pressure gradient force, marking a pronounced eastward acceleration. The expanded area (NG=7) also exhibited dominance of the eastward ageostrophic forcing but only at the lowest levels, above which both the advection term and Coriolis forcing were able to offset the westward ageostrophic forcing (not shown). In general, the average net forcing in the expanded area was one order weaker than that in the inner core, but both showed eastward acceleration at the lower levels. The analyzed budgets tended to indicate that the combined effect of the topography was to retard the westward movement of the larger or smaller portion of the vortex circulation upon their approach. Without upstream blocking of the original vortex center, the translational speed of the vortex after landfall was considerably faster than its initial speed as can be seen in Fig. 19.

The vorticity budget analyses may also provide an explanation for the vortex center advection southward. However, we found that the vorticity budgets were subject to interpolation errors in the coordinate transformation and only indicated the relative importance of the vorticity generation mechanisms. In fact,
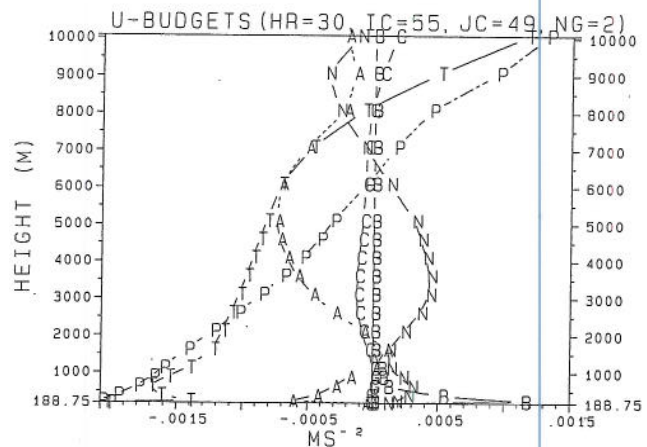

Fig. 22. As in Fig. 21(b) but for average u-momentum budgets.

the transformed vorticity budgets in the σ-coordinate were rather complex, particularly near the surface where the vertical wind shear was very large. As shown by the momentum budgets, the importance of the advection implied dominance of the vorticity advection and stretching as found by Yeh and Elsberry (1993b).

Smith and Smith (1995) also presented a leftward deflection as the upstream drifting vortex in the shallow water upon approaching the terrain. Lin et al.[†] have speculated the southward deflection in relation to upstream blocking of the flow and the channeling effects of the stronger northerly wind to the west of the center as the vortex center neared landfall. However, as shown in Fig. 19, the 3 km height vortex center was still deflected southward. From our v-momentum budgets where the net advection was northward, it is not clear how the northerly flow to the west of the center could offset the southerly advection and move the center southward. There should have been net southward forcing at some time for the southward movement of the major vortex circulation, and, intuitively, the sustained stronger northerly wind to the northwest prior to landfall seems to be a good candidate. The average north-south wind speeds of the large square-area ($NG=7$) in the inner vortex at 27 h were found to be northerly below a height of 5 km, with -0.104 m·s⁻¹ at 50 m, -1.467 m·s⁻¹ at 1 km, -0.917 m·s⁻¹ at 3 km, and a maximum speed of -1.82 m·s⁻¹ at 1.5 km. This maximum northerly wind resulted in a southward drifting deflection of about 40 km in 6 h, which is quite close to the deflection distance of two grid intervals between 24 h and 30 h as in the model results. However, the average low-level northerly wind at 30 h was not present for $NG=7$ but is for $NG=2$, indicating that the deflection was not supported by the broad vortex circulation extending to the leeside of the island (see Fig. 6). Hence, the net low-level northerly wind component existing during the track deflection time in our case was in consistent with the results of Bender et al. (1987), where a net low-level southerly wind component was closely related to the northward deflection in their simulations. Here, it seems to be easier to explain the track deflection in terms of the correlated wind component rather than its acceleration. However, it is also possible that the selective average zone in this study does not account for the vortex movement, and/ or that the track deflection is a complex nonlinear result that cannot be properly reflected by the average forcing. A more elaborate momentum analysis method needs to be developed to discover the inside complex dynamics responsible for the track deflection of smaller vortices.

The dynamic of vortex evolution is usually illustrated by the vorticity field. Recently, a potential vorticity concept has been brought into the modeling investigation as presented by Wu and Kurihara (1996) and Lin et al.[†] The interaction of a landfalling vortex with the terrain appears to be more complex in dynamic interpretation. Nevertheless, this study also provides some model results for the vorticity and potentail vorticity. Figure 23 shows the results of these two fields at a height of 100 m at 27 and 30 h (for reference, the horizontal winds are also plotted). Note that all the results presented in this figure are in σ-coordinates. In general, the geometric patterns of the vorticity and potential vorticity are similar, indicating that the low-level vortex dynamics may be well explained by the vorticity, and that the effect of vertical stability produces the dominant contribution. The potential vorticity was more concentrated than the vorticity in the vortex core. Negative regions appeared at the upstream slopes due to the blocking effect. The mountain blocking deformed the structure of the impinging vortex, which remains cyclonic. A prominent feature during these times is the region of positive vorticity and potential vorticity along the western slope, which moved further westward at 33 h as the vortex was deflected southeast of the slope (to be shown later).

The vertical structure of the impinging vortex are further shown by the cross-sectional results as shown for Case 1 in Fig. 24. The cross section is in the x-z plane and cuts through the vortex center. As can be seen, there is a remarkable similarity in the geometric distributions between the vorticity and potential vorticity. In this case, positive vorticity developed slightly higher than did positive potential vorticity. The suppression of the positive potential vorticity generation resulted from the destabilization effects in the overshooting region of the vortex core as can be seen in the 24 h results (see Fig. 10). Negative values of both fields were present in the outflow region of the upper-level vortex where anticyclonic vorticity contribution existed. Just over the upstream slope of the mountain, a negative strip region for both fields was also evident as shown in Fig. 23. In general, the concentrated vorticity field indicates that the impinging vortex remained well organized except near the surface where the blocking effect of the mountain seem to dominate the vorticity transport. At the downslope side, small positive vorticity was generated but only in the very thin layer attached to the slope since the vortex flow circulated primarily along the mountain during the time.

[†]Lin, Y. L., D. W. Hamilton, and C. Y. Huang (1997) Influence of orography cyclones. Submitted to *J. Atmos. Sci.*
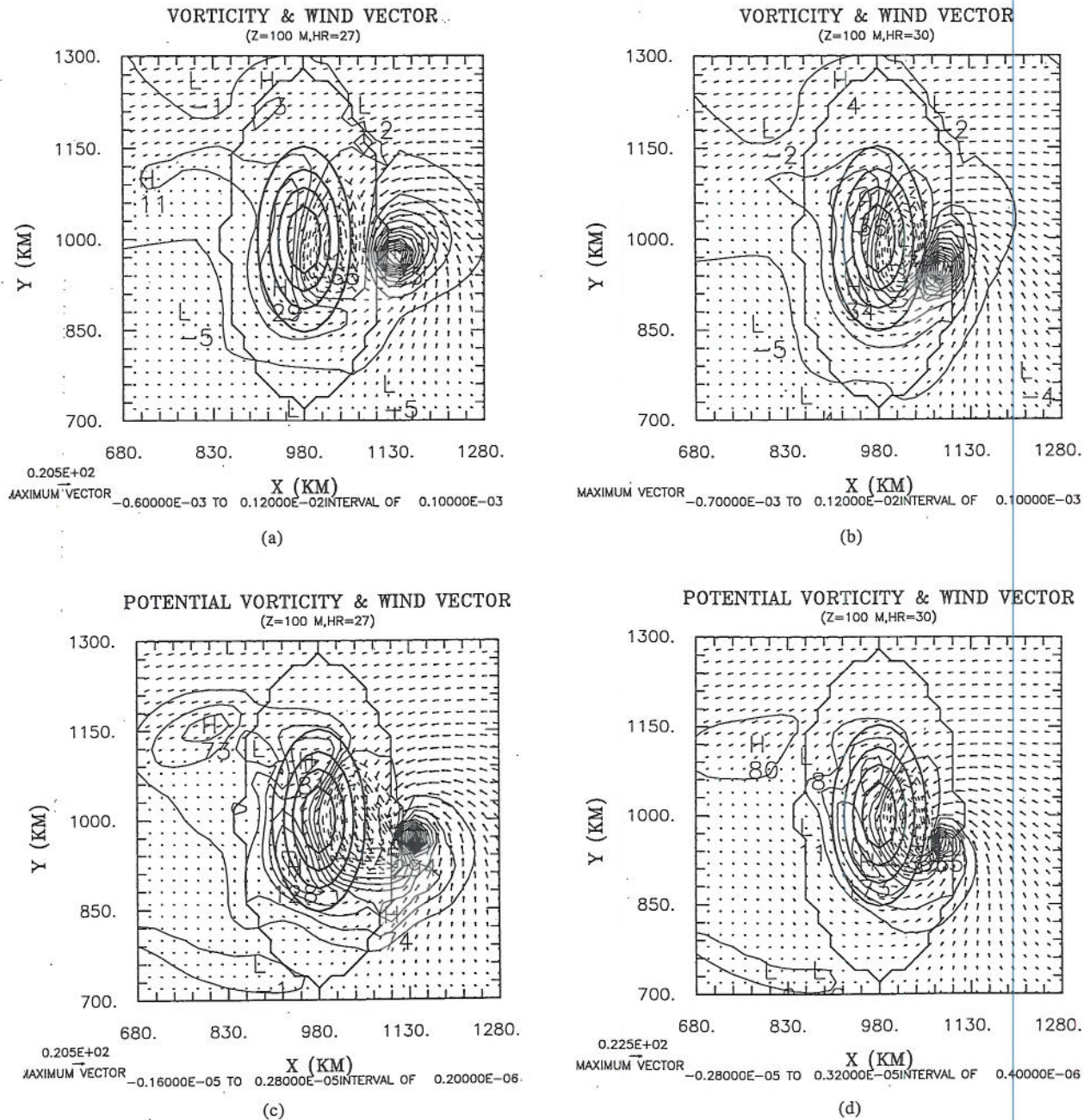
VORTICITY & WIND VECTOR
(Z=100 M,HR=27)

0.205E+02
MAXIMUM VECTOR −0.60000E−03 TO 0.12000E−02 INTERVAL OF 0.10000E−03

(a)

VORTICITY & WIND VECTOR
(Z=100 M,HR=30)

MAXIMUM VECTOR −0.70000E−03 TO 0.12000E−02 INTERVAL OF 0.10000E−03

(b)

POTENTIAL VORTICITY & WIND VECTOR
(Z=100 M,HR=27)

0.205E+02
MAXIMUM VECTOR −0.16000E−05 TO 0.28000E−05 INTERVAL OF 0.20000E−06

(c)

POTENTIAL VORTICITY & WIND VECTOR
(Z=100 M,HR=30)

0.225E+02
MAXIMUM VECTOR −0.28000E−05 TO 0.32000E−05 INTERVAL OF 0.40000E−06

(d)

Fig. 23. (a) The horizontal wind and vertical vorticity at 100 m for Case 1 at 27 h, (b) as in (a) but at 30 h, (c) the horizontal wind and potential vorticity at 100 m for Case 1 at 27 h, and (d) as in (c) but at 30 h. The physical units for potential vorticity are K $m^{-1} \cdot s^{-1}$.

3. Secondary Low

Although this study did not particularly focus on the problem of secondary-low formation, the model results are beneficial to earlier understanding. An empirical orthogonal function (EOF) analysis of 82 observed westbound typhoons (Chang *et al.*, 1993) showed that lee secondary lows tended to occur only when the typhoon center was in a rather narrow region of southeastern Taiwan, whether the typhoon was strong or weak. According to the observational results (Wang, 1980; Chang *et al.*, 1993), one or several secondary lows may have been induced at the lee side of the island as westbound typhoons neared land. As mentioned previously, secondary lows have been well simulated using several different models (e.g., Bender *et al.*, 1987; Chang, 1982; Yeh and Elsberry, 1993a; Cho *et al.*, 1996; Wu and Chuo, 1996). The types of modeled
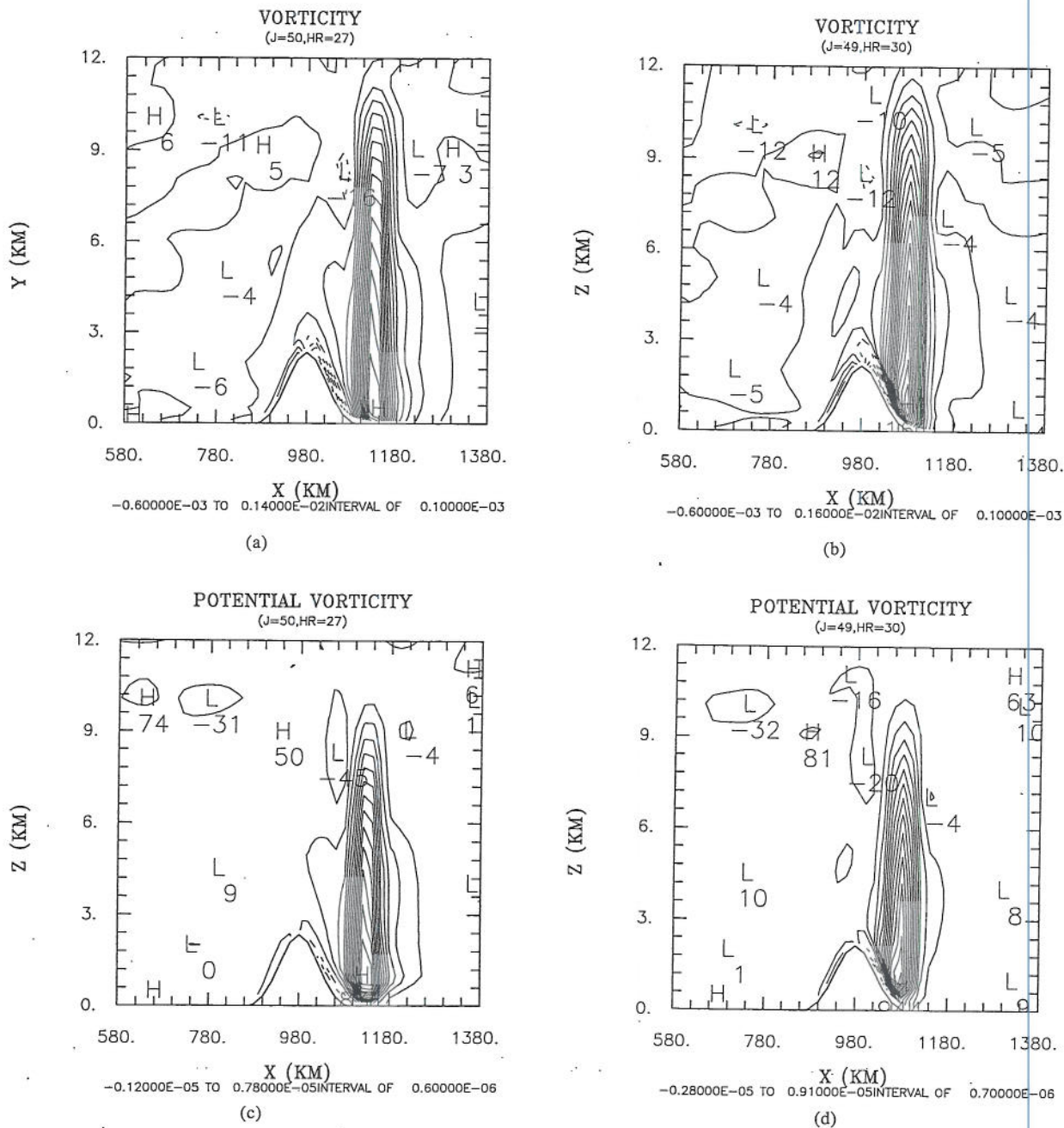
VORTICITY
(J=50,HR=27)

VORTICITY
(J=49,HR=30)

−0.60000E−03 TO 0.14000E−02 INTERVAL OF 0.10000E−03

(a)

−0.60000E−03 TO 0.16000E−02 INTERVAL OF 0.10000E−03

(b)

POTENTIAL VORTICITY
(J=50,HR=27)

POTENTIAL VORTICITY
(J=49,HR=30)

−0.12000E−05 TO 0.78000E−05 INTERVAL OF 0.60000E−06

(c)

−0.28000E−05 TO 0.91000E−05 INTERVAL OF 0.70000E−06

(d)

Fig. 24. The *x-z* cross-sectional results of Case 1 for (a) vertical vorticity at 27 h, (b) as in (a) but at 30 h, (c) potential vorticity at 27 h, and (d) as in (c) but at 30 h. The *x-z* cross section cuts through the vortex center. Note that the results at the lowest two levels are not plotted.

secondary lows have varied with complex dynamics and require careful inspection in each case. For example, Yeh and Elsberry (1993b) proposed that some secondary lows may develope as an upward growth of the low-level vorticity and replace the original vortex center, and that some may be taken over through downward extension of the upper level vorticity once the original vortex center passes over the mountain.

The model results show that the outer vortex

circulation surrounded the island during the track deflection time, as can be seen in Figs. 6 and 7. A close-up picture of the island circulation at 33 h is shown in Fig. 25. As seen, the original vortex center was in the southeastern region of the steep mountain, associated with a secondary low to the middle western island. The horizontal winds associated with the vorticity at a 100 m height (the third vertical level) are shown in Fig. 26. The vorticity pattern at near-surface (not
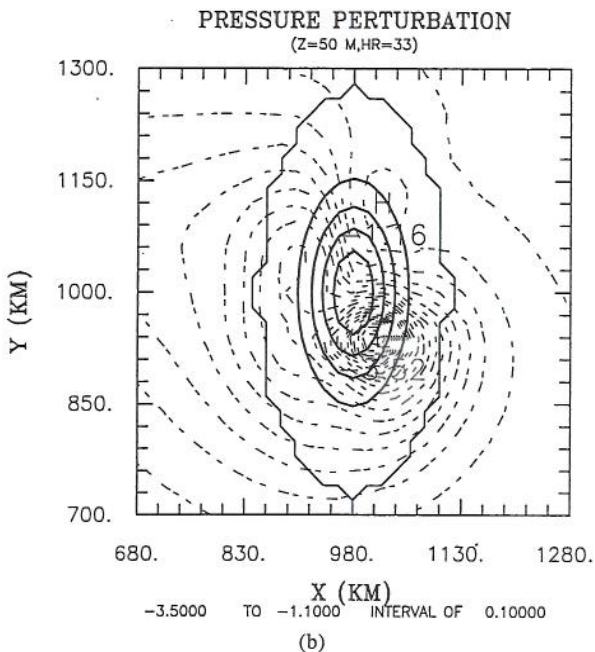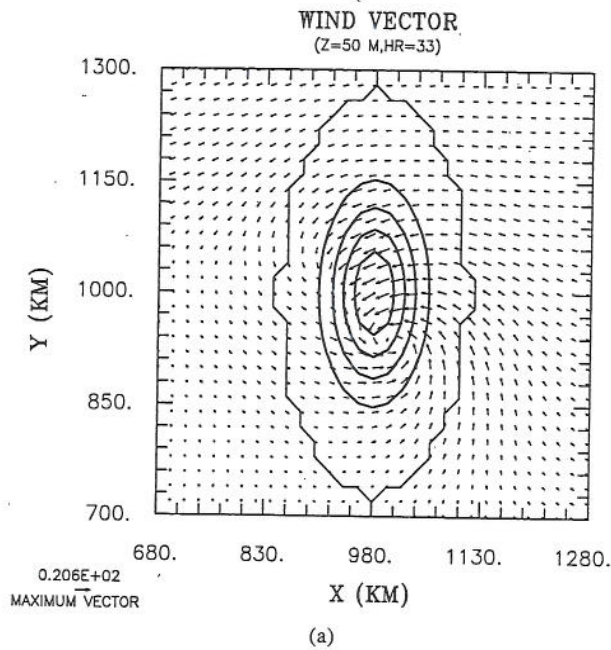
WIND VECTOR
(Z=50 M,HR=33)

0.206E+02
MAXIMUM VECTOR

X (KM)

(a)

PRESSURE PERTURBATION
(Z=50 M,HR=33)

-3.5000   TO   -1.1000   INTERVAL OF   0.10000

X (KM)

(b)

Fig. 25. The simulation results at a 50 m height for Case 1 at 33 h. (a) the horizontal wind, (b) the pressure perturbation with a contour interval of 0.1 mb.

VORTICITY & WIND VECTOR
(Z=100 M,HR=33)

0.232E+02
MAXIMUM VECTOR

0.00000E+00 TO 0.12800E-02INTERVAL OF 0.80000E-04

X (KM)

Fig. 26. The horizontal wind and vertical vorticity at 100 m for Case 1 at 33 h. The contour interval for the vorticity is 0.0008 s^{-1}. Maximum wind speed is 23.2 $m \cdot s^{-1}$.

northwest of the vortex. Note that the negative regions at 27 h and 30 h disappeared at 33 h as the vortex became more integrated above the slope.

The modeling position of the secondary low is in good agreement with observations (see Fig. 1(d) of Yeh and Elsberry, 1993b). For this case, the secondary low did not first appear as a pronounced cyclone, probably due to the tiny and weak outer vortex circulation. However, the transient flow at the secondary low developed quickly as a cyclonic vortex at 36 h when the 3 km vortex center neared. In this case, the upstream original near-surface center did not disappear.

Our model results seem to agree with the observational findings of Chang et al. (1993). Based on detailed analyses, Wang (1980) suggested that the secondary low was related to the adiabatic warming of the downslope wind. There is no doubt that the strong downslope wind crossing the mountain peak, shown in Fig. 24, is a beneficial factor for formation of the secondary low. For uniform upstream flow past an isolated mountain as in the Taiwan topography, the formation mechanisms of the meso vortex at the leeside have been attributed to vorticity stretching (e.g., Sun et al., 1991) or to vorticity tilting in the inviscid flow through baroclinic processes (e.g., Lin et al., 1992). However, the evolution of the secondary low in this vortex case can not be explained solely by either of the above mechanisms since no uniform upstream flow is maintained. Lin et al.[†] found that there was a close link between the severe downslope wind and the vor-

shown) is similar to that in Fig. 26 but with considerably larger magnitudes in the slope regions due to the strong vertical shear. As expected, positive vorticity was significantly produced in the inner vortex. A bent positive vorticity field resulting from the downslope wind is also evident. The low was slightly located to the outer region of the bent vorticity field
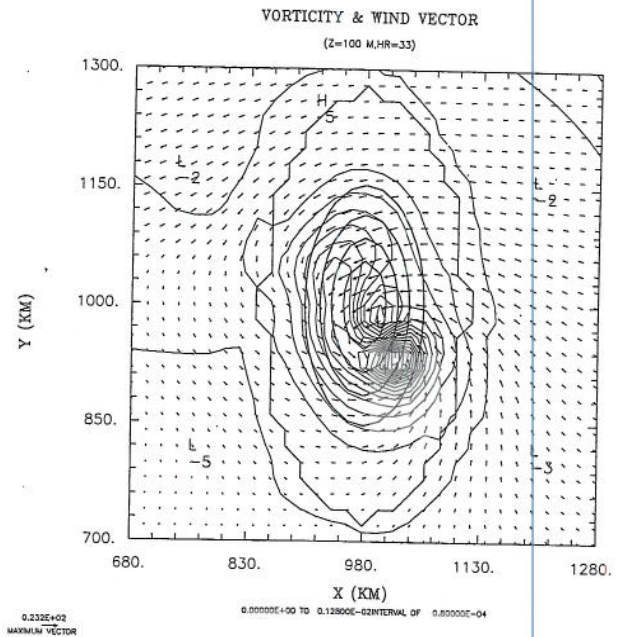
ticity strengthening as the vortex translated over the terrain, and that the rapid increase of the severe downslope wind was coexistent with the hydraulic jump in the inviscid flow. In other words, there was a flow transition regime from a splitting flow to an intense downslope wind or jump. Hence, in the latter flow type, there was potential vorticity generation as breaking mountain waves occurred.

While it appears to be more complex in the secondary-low development with the full boundary-layer physics in this study, some vorticity transport mechanisms may have been involved in the low evolution as the vortex turned southward around the steep slope and enhanced the cross-mountain flow, which was just at the radius of the strongest inner vortex region. This enhanced downslope wind in turn strengthened the vorticity generation and aided evolution into a new vortex where the old lee low was formed. Hence, both vorticity transport and vertical stretching could be two coexisting sources responsible for formation of the secondary lee vortex as discussed by Yeh and Elsberry (1993b) and Cho et al. (1996). In terms of potential vorticity, the PV source from nonlinear mixing by breaking mountain waves also provides another consistent explanation for the secondary-low formation in the case of inviscid flow as suggested by Lin et al.[†] It should be noted that different conclusions have been made based on different model assumptions and simulation parameters. The formation mechanisms of observed secondary lows remain to be discovered and deserve continuing study.

V. Conclusions

This study has presented a numerical investigation of vortex-terrain interaction using a native typhoon numerical model, which includes cloud microphysics and higher-order planetary boundary parameterization. In this comprehensive model, the seventh-order semi-Lagrangian advection scheme is employed to minimize numerical dissipation during long-term vortex revolutions. The numerical model has been applied to investigate the effects of island terrain on the track deflection of an idealized westbound vortex. The numerical results from idealized case simulations exhibit the evolution of the vortex as it approaches the island. It was found in tests that for a smaller size of vortex, whatever weak or strong, slow or fast, the vortex center was somewhat deflected southward prior to landfall and returned to its upstream original latitude and then kept moving straight westward.

The southward track deflection in this study differed from some previous results showing a northward deflection of a somewhat larger vortex (e.g.,

Chang, 1982; Yeh and Elsberry, 1993a, 1993b); however, it is consistent with the results of Lin et al.[†], in which prescribed heating was utilized to spin up the inviscid vortex to a size similar to that of the smaller vortex used in this study. In addition, Lin et al.[†] also found that the deflection of the typhoon track depended on its size, with a northward tendency for larger typhoons. Our preliminary results of a stronger and larger vortex from the same model also showed a northward deflection during landfall and will be reported in another paper.

The vortex initialization scheme solves the simple nonlinear-balance equation for a gradient wind, in which the horizontal distribution and vertical shear of a tangential wind are presumed. It was found that some prescribed winds at the gradient-wind balance could result in unrealistic vortex structures which can be, however, quickly modified by the model full-physics after the time integration. Hence, this initialization scheme works to constraint an expected vortex in size and intensity, but is unable to create a precise one. We also found that the vortex development was sensitive to the ambient moisture conditions, and that a dryer gradient-wind balanced vortex tended to decay gradually within one day. With feasible ambient moisture conditions, the vortex may be sustained due to boundary-layer flux convergence.

The numerical tests tend to show the importance of reliable vortex modification in the model integration when an initial vortex is implanted. Despite the uncertainty of the vortex dynamics in the balance between internal dissipation and external forcing, some of our conclusions based on the model simulations are, consistent with those of other modeling studies and with observations. There are many physical parameters which have not been addressed in this study. In justification of the complexity of the island-vortex interaction, lots of spaces, e.g., budget analyses of vorticity and potential vorticity in the σ-coordinate, are left for future investigation.

References

Anthes, R. A. (1982) Tropical Cyclones: Their Evolution, Structure, and Effects. Meteor. Monogr., Vol. 19, No. 41, p. 208. American Meteorological Society, Boston, MA, U.S.A.

Bender, M. A., R. E. Tuleya, and Y. Kurihara (1987) A numerical study of the effect of island terrain on tropical cyclones. Mon. Wea. Rev., 115, 130-155.

Brand, S. and J. W. Blelloch (1974) Changes in the characteristics of typhoons crossing the island of Taiwan. Mon. Wea. Rev., 102,

708-713.

Businger, J. A., J. C. Wyngaard, Y. Izumi, and E. F. Bradley (1971) Flux-profile relationships in the atmospheric surface layer. *J. Atmos. Sci.*, **28**, 181-189.

Chang, C. P., T. C. Yeh, and J. M. Chen (1993) Effects of terrain on the surface structure of typhoons over Taiwan. *Mon. Wea. Rev.*, **121**, 734-752.

Chang, S. W. (1982) The orographic effects induced by an island mountain range on propagating tropical cyclones. *Mon. Wea. Rev.*, **110**, 1255-1270.

Cho, S., C. Y. Huang, and Y. H. Kuo (1996) MM5 simulations of Dot Typhoon. *Chinese J. of Atmos. Sci.*, **24**, 123-144.

Davis, C. A. (1992) Piecewise potential vorticity inversion. *J. Atmos. Sci.*, **49**, 1397-1411.

Duynkerke, P. G. (1988) Application of the E-ε turbulence closure model to the neutral and stable atmospheric boundary layer. *J. Atmos. Sci.*, **45**, 865-880.

Duynkerke, P. G. and A. G. M. Driedonks (1987) A model for the turbulent structure of the stratocumulus-topped atmospheric boundary layer. *J. Atmos. Sci.*, **44**, 43-64.

Fiorino, M. and R. L. Elsberry (1989) Some aspects of vortex structure related to tropical cyclone motion. *J. Atmos. Sci.*, **46**, 975-990.

Huang, C. Y. (1990) *A Mesoscale Planetary Boundary Layer Numerical Model for Simulations of Topographically Induced Circulations.* Ph.D. Dissertation. Department of Marine, Earth and Atmospheric Sciences, North Carolina State University, Raleigh, NC, U.S.A.

Huang, C. Y. (1993) *Study of a Three-Dimensional Anelastic Nonhydrostatic Model* (in Chinese). Research Report, National Science Council, R.O.C., Taipei, R.O.C.

Huang, C. Y. (1994) Semi-Lagrangian advection schemes and Eulerian WKL algorithms. *Mon. Wea. Rev.*, **122**, 1647-1658.

Huang, C. Y. and S. Raman (1989) Application of the E-ε closure model to simulations of mesoscale topographic effects. *Boundary Layer Meteorol.*, **49**, 169-195.

Kessler, E. (1969) On the distribution and continuity of water substance in atmospheric circulations. *Meteorol. Monogr. No.*, **32**, 1-84.

Lee, C. S. (1991) The effects of Taiwan topography on landfall typhoons. *Proceedings of International Workshop on Mesoscale Research and TAMEX Program Review*, pp. 138-143, Taipei, R.O.C.

Lin, Y. L., N. H. Lin, and R. P. Weglarz (1992) Numerical modeling

studies of lee mesolows, mesovortices, and mesocyclones with application to the formation of Taiwan mesolows. *Meteor. Atmos. Phys.*, **49**, 43-67.

Mellor, G. L. and T. Yamada (1982) Development of a turbulence closure model for geophysical fluid problem. *Rev. Geophys. Space Phys.*, **20**, 851-875.

Miller, M. J. and A. J. Thorpe (1981) Radiation conditions for the lateral boundaries of limited area numerical models. *Quart. J. R. Met. Soc.*, **107**, 615-628.

Orlanski, I. (1976) A simple boundary condition for unbounded hyperbolic flows. *J. Comput. Phys.*, **21**, 251-269.

Peng, M. S. (1992) The typhoon track forecast system in the Central Weather Bureau and its performance during 1989-1991. *Proceedings of the Workshop on Recent Developments on Meteorology and Climatology in East Asia*, pp. 159-178, Chung-Li, Taiwan, R.O.C.

Smith, R. B. (1979) The influence of mountains on the atmosphere. *Adv. Geophys.*, **21**, 87-230.

Smith, R. B. and D. F. Smith (1995) Pseudoinviscid wake formation by mountains in shallow-water flow with a drifting vortex. *J. Atmos. Sci.*, **52**, 436-454.

Sun, W. Y., J. D. Chern, C. C. Wu, and W. R. Hsu (1991) Numerical simulation of mesoscale circulation in Taiwan and surrounding area. *Mon. Wea. Rev.*, **119**, 2558-2573.

Tsay, C. Y. (1993) Orography effects on the structure of typhoons: analyses of two typhoons crossing Taiwan. *TAO*, **5**, 313-333.

Wang, S. T. (1980) *Prediction of the Behavior and Strength of Typhoons in Taiwan and its Vicinity* (in Chinese). Research Report 108, National Science Council, R.O.C., Taipei, R.O.C.

Wu, C. C. and Y. C. Chuo (1996) Numerical simulation and observational analysis of Gladys Typhoon (1994) and the influence by Taiwan topography. *Proceedings of the Workshop on National Atmospheric Research*, pp. 340-349. Taipei, R.O.C.

Wu, C.C. and Y. Kurihara (1996) A numerical study of the feedback mechanisms of hurricane-environment interaction on hurricane movement from the potential vorticity perspective. *J. Atmos. Sci.*, **53**, 2264-2282.

Yeh, T. C. and R. L. Elsberry (1993a) Interaction of typhoons with the Taiwan orography. Part I: upstream track deflection. *Mon. Wea. Rev.*, **121**, 3193-3212.

Yeh, T. C. and R. L. Elsberry (1993b) Interaction of typhoons with the Taiwan orography. Part II: continuous and discontinuous tracks across the island. *Mon. Wea. Rev.*, **121**, 3213-3233.

入侵對稱地形的中尺度渦旋之演變

黃清勇*　　林玉郎**

*國立中央大學大氣科學系
**美國北卡羅萊納州立大學海洋、地球暨大氣科學系

摘　　要

　　本文利用中尺度數值模式，探討入侵對稱地形的中尺度渦旋其環流演化過程。此數值模式包含高階邊界層參數化、雲物理過程及颱風模擬之初始化方法。爲配合長時間的颱風模擬，模式平流項計算使用高精確的高階半拉格朗日法以減少數值衰減。本文理想化個案模擬結果指出，對於由東入侵地形中心的渦旋如較小型颱風，無論其快或慢，強或弱，其中心路徑於登陸中尺度對稱地形時有向南偏移現象，於過山後逐漸拉回至約原中心線。動量收支分析指出，此南偏現象最有可能爲南向的非地轉氣壓梯度力分量所致。當渦旋中心登陸期間，亦受東向的非地轉氣壓梯度力分量所阻，此時在地形下游產生一副低壓中心。此副中心伴隨強烈的下坡風，此有利於渦度之生成。其隨後爲移速明顯加快的原中心所取代，形成一新的渦旋中心，然後以直線繼續西移。